Utrecht University

Faculty of Geosciences

Department of Physical Geography

A new methodology for measuring ice cliff backwasting rates on debris-covered glaciers using high-resolution unmanned aerial vehicle imagery

A thesis submitted in partial fulfillment of the requirements for

Master's degree in Earth Surface and Water

<table>
<tr><td>*Author:*</td><td>*Supervisors:*</td></tr>
<tr><td>Tim Busker</td><td>Dr. Walter Immerzeel</td></tr>
<tr><td>t.s.busker@students.uu.nl</td><td>Philip Kraaijenbrink MSc</td></tr>
<tr><td></td><td>Jakob Steiner MSc</td></tr>
</table>

Utrecht

January, 2017

Abstract

Ice cliffs potentially contribute considerably to the glacier mass balance, as melt enhancement on ice cliffs was observed by multiple recent studies. However, quantification of ice cliff melt is still in its infancy. Distributed models are still very computationally intensive and no methodology exists that allows for the direct measurement of ice cliff backwasting. This study therefore developed a new methodology to directly measure ice cliff backwasting on high-resolution UAV imagery with the Multiscale Model to Model Cloud Comparison (M3C2) algorithm. Two sets of experiments showed that a normal scale of 20 m in combination with a horizontal constraint of the normals in average backwasting direction resulted in accurate cliff backwasting values. The technique allowed cliff-to-cliff measurements with a RMSE of only 0.4 m. Backwasting patterns were generated for five cliffs on the Nepalese Langtang glacier for the period May 2014 - October 2015, which revealed an average backwasting rate of 10.5 m a^{-1}. The rate is 13 times higher than the average ablation of 0.8 m a^{-1} on this part of the glacier tongue and could be an important explanation for the observed debris-cover anomaly. The backwasting rate varied considerably among different parts of the cliffs and between different cliffs, which could be well explained by the influence of aspect and supraglacial ponds. Supraglacial ponds caused a consistent positive melt gradient from cliff top to base, indicating a large role of thermal erosion in the ablation and development of ice cliffs. The M3C2 algorithm was applied to an additional cliff on Lirung glacier, which showed similar backwasting values as found by previous studies on that cliff. The methodology developed in this study is faster and probably less complex than other studies measuring or modelling ice cliff backwasting. The temporal and spatial scalability of the methodology will improve accurate assessment of a glacier's mass balance: the melt contribution of ice cliffs is finally revealed through detailed backwasting patterns. Automatization of the different steps in this research is recommended to facilitate this process.

Keywords: Debris-covered glaciers, ice cliffs, supraglacial ponds, UAV, M3C2, backwasting

Acknowledgements

I would like to thank my supervisors from Utrecht University, dr. Walter Immerzeel, Philip Kraaijenbrink MSc and Jakob Steiner MSc, for their excellent support and feedback during the complete period of this research. They steered me correctly to the right direction whenever this was necessary, but still allowed me to apply my own and creative ideas in the analyses. Their support was gratefully acknowledged. I also would like to thank Fanny Brun (Université Grenoble Alpes) for kindly sharing her interesting ideas about measuring ice cliff backwasting. Writing this thesis would not have been possible without the extraordinary good help, guidance and support from these people. Thank you.

Table of Contents

1. Introduction

The Himalayan mountain range extents over 2000 km from Afghanistan to Burma, formed during the collision of the Eurasian and Indian plates. Globally it is one of the most important and most glacialised areas, but also one of the least understood (Hambrey et al., 2009). Himalayan glaciers play a vital role in the Asian water cycle, supplying water for many Asian regions. They provide a valuable source of water for millions of people that are dependent on this water for drinking, food security, hydropower potential and sanitation (Immerzeel, Pellicciotti, & Bierkens, 2013; Immerzeel, van Beek, & Bierkens, 2010; Schaner, Voisin, Nijssen, & Lettenmaier, 2012). Climate change will alter these water supplies, by changing precipitation patterns, glacier and snow runoff. Glaciers are very sensitive to climate change. Except for the Karakoram mountain range, all glaciers in High Mountain Asia (HMA) have experienced a mass loss in last decades (Bolch et al., 2012; Julie Gardelle, Berthier, & Arnaud, 2012; Kääb, Treichler, Nuth, & Berthier, 2015). This mass loss is generally accompanied by a reduction in the glacier area and deceleration of glacier flow, which causes the majority of ablation areas in the Himalaya to be nearly stagnant (Luckman, Quincey, & Bevan, 2007; Quincey, Luckman, & Benn, 2009; Seko et al., 1998). These processes will increase the glacier runoff for the Himalayas until at least 2050 (Immerzeel et al., 2013). Together with an increasing trend in precipitation, this will not endanger water availability in downstream areas towards the end of this century (Immerzeel et al., 2013). However, the total glacier volume will decline and this will cause declines in glacier melt runoff for most Himalayan areas after 2050. The rivers will become more nival and pluvial with more variable and direct discharge, because of a reduced buffering effect of the glacier reservoirs and more rainfall (Agrawala, Raksakulthai, Larsen, Smith, & Reynolds, 2003). Understanding Himalayan glaciers will therefore be crucial for designing future water management policies, especially since water demand is projected to increase significantly in most Asian river basins (Immerzeel & Bierkens, 2012).

1.1 Debris-covered glaciers

Himalayan glacier tongues are typically characterized by a thick debris cover (Immerzeel et al., 2014; Ragettli, Bolch, & Pellicciotti, 2016). Understanding these debris-covered glaciers is crucial for understanding and modelling glacier response to climate change in Asia. Debris-covered glaciers account for about 10 % of all glaciers in High Mountain Asia (HMA) and this ratio increases to 25-36 % in the Nepalese Himalayas (Nuimura et al., 2012; Shea et al., 2015; Thakuri et al., 2014). The majority of ice in the Himalayan mountains is stored in glaciers having more than 20 % debris cover (Bolch et al., 2012; Miles et al., 2016; Scherler, Bookhagen, & Strecker, 2011). These glaciers are normally located at lower elevations than clean ice glaciers, therefore contributing significantly to total mass loss in the Himalayan mountains. Moreover, the debris-covered surface area is projected to increase in the near future, driven by an increasingly negative mass loss (Buri, Miles, & Steiner, 2016b). These glaciers are common in almost all other mountain ranges in the world (Brun et al., 2016; M. P. Kirkbride, 1993; Ogilvie, 1904; Scherler et al., 2011). Understanding debris-covered glaciers is therefore crucial for understanding the glaciological response to global warming.

Melt on debris-covered glaciers can occur on (1) clean ice, (2) beneath the debris cover, (3) ice cliffs in combination with calving or (4) calving into large proglacial ponds near the glacier moraine (Benn et al., 2012). These different melting processes result in inhomogeneous surface ablation, which make mass loss patterns more complex. The main source of supraglacial debris is mass movement from the slopes just besides the glacier, such as erosion from the lateral moraines, rock avalanches, debris flows, rockfall and ice/snow/rock avalanches (Hambrey et al., 2009; M. P. Kirkbride, 1993). Debris cover is more likely to persist in the ablation zones than in accumulation zones of a glacier. These glacier tongues are generally characterized by low flow velocities and a high supply of debris from adjacent mountain slopes originating from weathering and erosion, which stimulates the formation of a debris

cover (Barsch, 1992; M. Kirkbride, 2011). Moreover, supraglacial debris in the accumulation zone will generally be entrained into the ice mass, while emergent flow in the ablation area will generally keep the supraglacial debris on the glacial surface. Therefore, the debris is supraglacially concentrated in ablation areas and regularly forms a near-continuous debris mantle (Hambrey et al., 2009). The debris mantle is important for the geomorphology of the glacier, since accumulated debris in depressions trigger relative uplift of these areas by lowering the melting rate. This 'basin inversion' is the main process causing local depressions to accumulated and local hills to ablate, resulting in a hummocky appearance of most debris-covered glaciers (Hambrey et al., 2009).

The way in which debris cover changes ablation rates is studied since the late 1950s (Suzuki, 2011). A thin and dispersed debris cover (1.5 to 8.0 cm or less) is assumed to increase melting rates, since it will lower the albedo and enhance the availability of longwave radiation to melt (Bolch, 2011; Nakawo & Young, 1981; Östrem, 1959; Suzuki, 2011; Tangborn & Rana, 2000). Because of the low thermal conductivity of debris, a thick debris cover causes insulation and reduces melting rates (M. Kirkbride, 2011; Östrem, 1959). The debris thickness for which the debris-covered melt rate is the same as the melt rate observed on bare ice glaciers, is called the critical thickness (Suzuki, 2011). The critical thickness was experimentally deduced on 9.0 cm by (Rana, Masayoshi, Yutaka, Kubota, & Kojima, 1998) and on 0.5 cm by Östrem (1959). The values for the critical thickness and maximum melt differ in different situations, since melt is dependent upon multiple other external (air temperature, radiation, albedo) and internal (thermal conductivity) processes (Nakawo & Young, 1981). However, for almost all debris-covered glaciers the debris thickness is much larger (from 50 to 200 cm) than this critical thickness (Hambrey et al., 2009). Hence lower melting rates should be expected on these glaciers than on bare ice glaciers. Many large-scale geodetic studies using remote sensing nevertheless suggest debris-covered glaciers to melt as fast as, or faster than, debris-free glaciers (J. Gardelle, Berthier, Arnaud, & Kääb, 2013; Kääb, Berthier, Nuth, Gardelle, & Arnaud, 2012; Nuimura, Fujita, Yamaguchi, & Sharma, 2012). This antinomy is called the debris-cover anomaly (Pellicciotti et al., 2015).

1.2 Melting mechanisms on ice cliffs

Tongues of debris-covered glaciers are usually covered with many supraglacial ponds and ice cliffs, which marks the glacier's response to climatic changes (Figure 1.1) (Benn et al., 2012). The role of their ablation was underestimated for a long time. Recent studies, however, suggest considerably higher melting rates around ponds and ice cliffs, compared to other areas on the glacier (Brun et al., 2016; Buri, Pellicciotti, Steiner, Miles, & Immerzeel, 2016a; Immerzeel et al., 2014). The melt on ice cliffs can be several meters in a single melt season (Benn et al., 2001). In Brun et al. (2016), the catalytic melting in these areas caused six times more melt than on relatively flat debris-covered glacier areas. Immerzeel et al. (2014) and Sakai, Nakawo, & Fujita (1998) reported a magnitude higher melt rate on cliff areas. Differencing of Digital Elevation Model's (DEM) is an often used tool for calculating this catalysing melt effect of ice cliffs (e.g. Bolch, Pieczonka, & Benn, 2011; Immerzeel et al., 2014). The melt acceleration in cliff-pond systems could be a possible explanation for the debris-cover anomaly (Brun et al., 2016) and is the main reason why debris-covered glaciers reveal higher melt rates than implied by the insulation effects of the debris (Buri et al., 2016a ; Steiner et al., 2015). However, discussion remains whether these melt magnifications can cause debris-covered glaciers to melt as fast as debris-free glaciers. Ragettli et al. (2016) also found melt enhancement in cliff-pond systems, but this melt could not compensate for the insulating effect of the debris. The Yala glacier in the Langtang catchment showed melt rates up to 35-300 % higher than debris-covered glaciers (e.g. Langtang glacier) within the same altitude range (Ragettli et al., 2016). Vincent et al. (2016) found much lower ablation on the debris-covered Changri Nup Glacier (ca. 1.8 m w.e. a^{-1}), compared to bare-ice glaciers in the surrounding area, for the same reason. Therefore, their observations could not confirm the existence of the debris cover anomaly.

Figure 1.1 A picture of a typical cliff-pond system on the Langtang Glacier (Photo credits © Joseph Shea).

A couple of factors are responsible for the melt magnification in these cliff-pond systems. Cliffs are generally covered with a very thin dust layer, which is much thinner than the critical thickness. Especially in the melting season, the cliff surface can be very dirty (Benn et al., 2001). A consequently lower albedo causes more absorption of shortwave radiation. Moreover, the steep slopes of cliffs can be exposed to high amounts of radiation when faced to the south(west) on the Northern Hemisphere, since the solar zenith angle is small during the mid-day (Reid & Brock, 2014). Cliffs additionally receive thermal longwave radiation emitted from the surrounding debris, which warms significantly more at the surface than clean ice during the day. The proximity of a pond further increases melt, by transferring heat towards the subaqueous cliff surface. Heat from a supraglacial pond is assumed to leave trough three different processes: (1) heat lost in the water outflow, (2) latent heat for ice melt under the debris layer and (3) latent heat for bare ice melt. The latter two processes are responsible for very high subaqueous melt rates, which can be an order of magnitude higher than subaerial melt (Benn et al., 2012). In this way, supraglacial ponds can create significant slope steepening and eventually create undercuts at areas of (formerly) submerged ice. This can in turn cause calving of several meter tall ice blocks, which could increase cliff ablation threefold (Benn et al., 2001; Hambrey et al., 2009). Therefore, supraglacial ponds are suggested to be of crucial importance for the fate and state of ice cliffs (Benn et al., 2012; Benn et al., 2001; Buri et al., 2016b; Kraaijenbrink et al., 2016). Subaqueous melt is stimulated by (1) free convection due to temperature-dependent density differences (Eijpen, Warren, & Benn, 2003) and (2) valley-wind driven water currents with enough fetch (Miles et al., 2016; Sakai, Nishimura, Kadota, & Takeuchi, 2009). Wind driven water currents are suggested to control thermal undercutting. Large supraglacial ponds (>80 m long) have a large fetch and are therefore assumed to produce more undercutting and calving than small ponds (Sakai et al., 2009). Scott Watson et al. (2017) however, also found calving on ice cliffs adjacent to smaller ponds than 80 m.

To understand the evolution of ice cliffs and their backwasting patterns, it is important to understand all radiation fluxes from and to the cliff surface. The radiation balance is defined by the balance between ingoing and outgoing radiation and can be summarized in the following equation:

$$Q_m = I_n + L_n + \text{H} + \text{LE} \tag{1}$$

Where Q_m is the energy available for melt, I_n and L_n are the net shortwave and net longwave radiation fluxes respectively, LE is the latent heat flux and H represents the sensible heat flux. Buri et al. (2016a) further specified the shortwave and longwave fluxes into six different forms in which they can reach the cliff surface: (1) direct shortwave radiation from sky, (2) diffuse shortwave radiation from sky, (3) shortwave radiation reflected by the terrain, (4) longwave radiation emitted from the surrounding terrain, (5) longwave radiation emitted from the ice and (6) atmospheric longwave radiation. The

distribution of these radiation fluxes differ quite significantly among different locations on the cliff and among different cliff aspects (Kraaijenbrink et al., 2016; Steiner et al., 2015). Cliff surroundings can block direct shortwave radiation before it reaches the cliff surface, especially at times of a low solar zenith angle. Since this effect will be larger at the bottom of the cliffs compared to the top, relatively more solar radiation will reach the cliff top than the cliff base. However, this radiative deficit at the cliff base is partly offset by a higher debris-view factor, which is the amount of debris compared to the amount of sky as can be observed from a single point on the cliff (Steiner et al., 2015). A higher debris-view factor at the base increases the total amount of received longwave radiation from surrounding debris. Sakai, Nakawo, & Fujita (2002) therefore hypothesized that north-facing cliffs (on the northern hemisphere) will receive less solar radiation near the top because of self-shading effects, while they receive relatively much longwave radiation near the bottom emitted by surrounding debris. This would sustain north-facing cliffs, while south-facing cliffs disappear more quickly as they receive relatively more radiation at the top. Steiner et al. (2015) confirms self-shading on especially north-facing cliffs to be an important factor for cliff evolution. Scott Watson et al. (2017) found the aspect of 8229 ice cliffs on 14 different glaciers in the Everest region to be primarily north(west)-facing. South-facing cliffs on a part of the Langtang glacier tongue studied by Kraaijenbrink et al. (2016) are largely absent and the few south-facing cliffs always contained supraglacial ponds or a relatively low slope value to sustain them (Kraaijenbrink et al., 2016). These studies therefore strengthened the hypothesis of Sakai, Nakawo & Fujita (2002) that explains the survival mechanisms of north-facing ice cliffs.

Ice cliffs are subjected to seasonal variations in melt rates. Higher melt rates are found during the summer monsoon season (June to September), while generally lower melt rates are found during the winter season (November to May) (Brun et al., 2016). This can be explained by more incoming shortwave radiation, a higher surface temperature and a thin layer of debris on the melting cliffs during the summer monsoon season (Benn et al., 2012). Melt rates in the post-monsoon period (October) are lower than in the pre-monsoon period (May), because of similar reasoning (Steiner et al., 2015).

1.3 Development of cliff-pond systems

Although cliffs and ponds are often found together, both ice cliffs and supraglacial ponds can also persist individually (Kraaijenbrink, Shea, Pellicciotti, de Jong, & Immerzeel (2016). However, a considerable spatial coincidence between ice cliffs and ponds is observed (Scott Watson et al., 2017).

Supraglacial ponds are primarily formed on higher elevations than the glacier outlet. Benn et al. (2001) made a crucial distinction between perched ponds and base-level ponds, which is based on the location relative to the glacier outlet. Perched ponds are found on elevations above the glacier outlet, while base-level ponds develop at the same altitude as the glacier outlet. Perched ponds can only exists if they are underlain by an impermeable, unfractured ice layer with a low permeability (Benn et al., 2012; Jordan & Stark, 2001). Besides factors as velocity and slope, their development can potentially be linked with internal glacier movement. Kraaijenbrink et al. (2016) found high pond densities near confluences on the Langtang glacier, probably caused by transverse compressions that close englacial conduits, hamper drainage and therefore stimulate pond formation. They are sometimes connected to the englacial drainage system and rarely become bigger than a diameter of 100-200 m before drainage occurs (Benn et al., 2012; Immerzeel et al., 2014). Pond temperatures are estimated to be around 3 °C during summer and early autumn, which is relatively warm compared to other parts of the glacier (Sakai et al., 2009; Sakai, Takeuchi, Fujita, & Nakawo, 2000). This warm pond water causes ice melt by interaction at the pond-ice interface as well as by drainage through the englacial hydrological system. Drainage is assumed to be accelerated by the relatively high water temperature, which causes thermal enlargement of the englacial conduits (Miles et al., 2016; Sakai et al., 2000). Some cliff-pond systems reveal several cycles of drainage and filling (Benn et al., 2012). Immerzeel et al. (2014) hypothesized that these cycles can be steered by the melting of englacial conduits during summer monsoon, which are frozen during winter. This should explain the frequently observed pond drainage between May and October 2013 on the

Lirung glacier (Immerzeel et al., 2014; Miles et al., 2016). Besides drainage through the englacial drainage system, the pond water level can further change due to variations in precipitation, evaporation and meltwater supply. Ice calving or debris fall can also add mass to the pond, resulting in rising pond water levels (Benn et al., 2001).

Supraglacial ponds are assumed to be of major importance in the sustainment and development of ice cliffs. The locations of the cliffs generally correspond with areas of low inclination, significant downwasting and a low velocity (Immerzeel et al., 2014; Miles et al., 2016). They are formed by three main processes: (1) debris slumping when the slope becomes steeper, (2) calving of the ice into an adjacent pond and (3) collapsing of a conduit roof creating a funnel-shaped hollow (Benn et al., 2012, 2001; Kirkbride, 1993). The latter process triggers a positive feedback loop, meaning that the development of certain cliff-pond systems can stimulate the development of other systems. The earlier mentioned thermal conduit enlargement caused by drainage of warm pond water can create conduits which become too large to carry the above laying glacier mass. A hypothesis suggests that they can collapse and create a funnel-shaped hollow. These hollows could be ideal places for new ice cliffs or ponds to form (Benn et al., 2012; Sakai et al., 2000). This was strengthened by modelling efforts for a supraglacial pond on the Lirung glacier, in which conduit enlargement because of melting of 2612 m^3 ice was modelled (Miles et al., 2016).

1.4 Quantifying ice cliff backwasting

Ice cliff backwasting is defined as the movement of ice cliffs in an approximately horizontal direction because of melting on its surface. Due to accelerating melt rates found for cliff-pond systems, it is crucial to develop techniques and models that allow for measuring and simulating ice cliff backwasting. However, the quantification and understanding of melt in cliff-pond systems is still in its infancy, mainly because of inaccessibility in the field and the lack of in situ measurements.

1.4.1 Modelling studies

Most recent attempts for quantifying ice cliff backwasting have been conducted using high-resolution Unmanned Aerial Vehicle (UAV) data. This is a complicated process that is mostly attempted by using numerical models. Most of these models focused on point-scale modelling that estimates melt by modelling the radiative transfer for one point on the cliff surface (e.g. Han, Wang, Wei, & Liu, 2010; Reid & Brock, 2014; Sakai et al., 1998, 2000; Steiner et al., 2015). Note that Steiner et al. (2015) used grid-based radiative fluxes, resulting in point-scale cliff backwasting rates. Therefore, also this model is still a point-scale model (Steiner et al., 2015). All of these models (except Steiner et al. (2015)) have extrapolated these point estimates to calculate mean cliff melting and the contribution of ice cliffs in the total mass balance of the glacier. The first fully distributed model (represented by a 0.2 m raster) has been published by Buri et al. (2016a), which builds on the point model of Steiner et al. (2015). This model is a large step forward in the understanding of cliff-pond systems, since it can more accurately quantify the ablation on the whole cliff, rather than extrapolating point estimates. However, this model does not include the effect of supraglacial ponds, is based on a static cliff geometry and does not account for reburial of cliffs by debris (Buri et al., 2016a). Therefore, an improvement of this model has been published recently that allows for a monthly update of the cliff geometry as implied by the calculated melt (Buri et al., 2016b). This model additionally includes the effect of supraglacial ponds and reburial by debris. They discovered that these factors are very important for the evolution of ice cliffs (Buri et al., 2016b).

1.4.2 Distance measurement techniques

Three techniques are commonly used for comparing point clouds or DEMs, which are (1) DEM of difference (DoD), (2) cloud-to-cloud comparison with closest point technique (C2C) and (3) cloud-to-mesh distance (C2M). Lague, Brodu, & Leroux (2013) developed a new algorithm for direct distance calculations on 3D point clouds, which could be very promising for measuring ice cliff backwasting. All four techniques will be evaluated below on the purpose of measuring ice cliff backwasting.

Cloud-to-cloud (C2C) and cloud-to-mesh (C2M) technique

The C2C technique looks very promising for comparing different point clouds. It is a relatively simple and fast technique which does not require the development of a grid, mesh or surface normals (Lague et al., 2013). The algorithm searches for each point in the compared point cloud (equivalent to t_2 in this research) the closest point in the reference point cloud (or t_1) (Figure 1.2A). A more advanced option of this algorithm allows for the generation of a local model on the reference surface S_1 (Girardeau-Montaut, 2015). The local model represents an average local (planar) surface generated by all neighboring points within radius r_m from the closest point in point cloud 1 (Figure 1.2B). This local model is especially effective if a point cloud is not dense enough (Girardeau-Montaut, 2015). Another distance technique is the C2M-distance, which will generate a mesh from the reference point cloud. For each point in the compared point cloud, it will simply search for the nearest triangle in the reference mesh (Figure 1.2C) (Cignoni, Rocchini, & Scopigno, 1998).
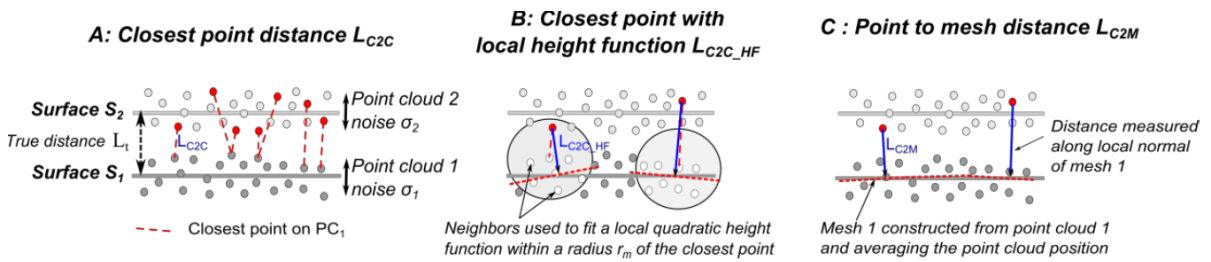

Figure 1.2A: The simple C2C closest point algorithm searches for each point in point cloud 2 the closest point on point cloud 1 and calculates the distance (L_t) **Figure 1.2B:** The local C2C-distance is the distance between a point in point cloud 1 and a local plane in point cloud 2. **Figure 1.2C:** Using the C2M-distance, all points in point cloud 2 will measure the closest distance to a mesh (dotted red line) derived from point cloud 1 (Lague et al., 2013).

Both the C2C as C2M algorithm are not effective for measuring ice cliff backwasting. Cliffs can have a rough surface and can even contain undercuts. By choosing the closest point for the distance measurement, the algorithm systematically underestimates the distance at rough cliff surfaces and undercuts. The algorithm will never be able to reach the furthest parts of these surface features, since it will often find a closer point (or triangle for the C2M) on the reference surface S_1. In addition, the methodology is very sensitive to cloud outliers and point spacing (Lague et al., 2013).

DEM of difference (DoD)

When the geometry of the point cloud is planar and consists primarily of horizontal surfaces, the DoD technique can be very fast and accurate (Lague et al., 2013). The point clouds are gridded to generate two DEMs, which are subtracted from another on a pixel-by-pixel basis. This can be very effective when assessing vertical elevation differences and it is therefore often used in estimating planimetric elevation changes over the entire glacier (Berthier, Schiefer, Clarke, Menounos, & Rémy, 2010; Bolch, Buchroithner, & Pieczonka, 2008; Bolch et al., 2011; Immerzeel et al., 2014). Although this technique is suitable for providing a rough estimate of total volume losses in cliff-pond systems, the

technique cannot generate accurate backwasting rates or spatial backwasting patterns, due to low information densities on steep vertical sections. The melting distance on steep cliffs should be measured along the nearly horizontal direction of the surface normals.

The Multiscale Model to Model Cloud Comparison (M3C2) algorithm

Lague et al. (2013) developed a new algorithm allowing direct comparison of 3D point clouds, named M3C2. Brun et al. (2016) stated the technique as promising for future analysis of spatial backwasting patterns. The technique calculates the distance using the direction of surface normals instead of simply measuring distance to the closest point (C2C technique) or in one uniform vertical direction (DoD technique). Since the algorithm contains spatially complex elements, the implementation of this algorithm on point clouds justifies a more detailed explanation.

The first step in the M3C2 algorithm is the calculation of a surface normal vector (N) for point i. The normal direction is perpendicular on the best fit plane, which is calculated using all neighboring points NN_i of point i located within normal scale D, or radius D/2 (Figure 1.3a, step 1). The distance between the neighbors NN_i and the best fit plane generates the standard deviation, or cloud roughness σ_i (D) at scale D. The calculated normals can be estimated on the reference cloud, the compared cloud or the average of both (Lague et al., 2013). In this research, the reference cloud represents the initial situation (t_1) and the compared cloud the final situation (t_2).

The next step is to project a cylinder of size d along normal direction N, which axis is projected through point i (Figure 1.3a, step 2). The scale of this cylinder is called the projection scale (d). The points of both the reference and compared point cloud located within the cylinder will be projected on the cylinder axis. The resulting average points correspond to i_1 (for the reference point cloud) and i_2 (for the compared point cloud). The distance between i_1 and i_2 finally gives the calculated local distance L_{M3C2} (i). A local cloud roughness estimate in the reference cloud (σ_1 (d)) and the compared cloud (σ_2 (d)) is also provided by the algorithm for the cylinder area and a maximum cylinder length must be set to speed up the calculation (Lague et al., 2013). This process must be conducted for every single point in the point cloud.
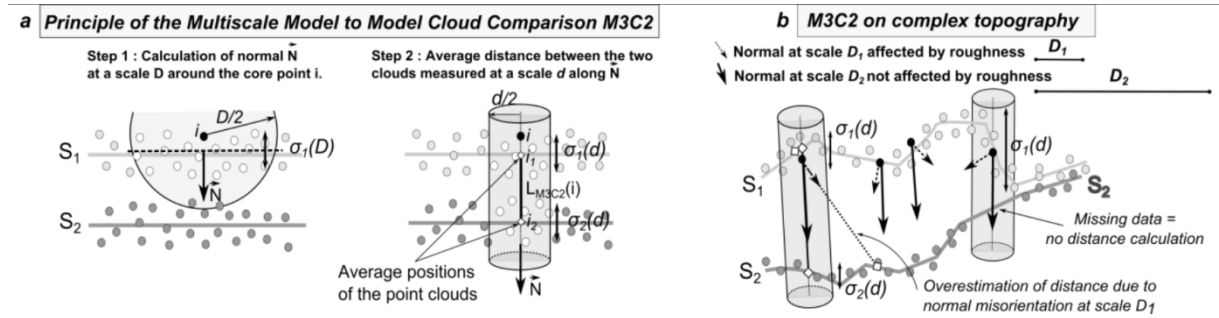

Figure 1.3a: An illustration of calculating the normal orientation N (step 1) and projecting the cylinder at projection scale d, that calculates the average positions i_1 and i_2 and derives the distance between them ($L_{M3C2}(i)$) (step 2). **Figure 1.3b**: The calculated distance is very sensitive to the size of normal scale D. The normal scale must be big enough to overcome small scale roughness (e.g. scale D_2), since a too small scale can result in overestimations due to scattered normals (e.g. scale D_1). Scale D_2 would suite best in most cases, since the change is unlikely a result of small scale roughness (Lague et al., 2013).

This research developed its own reference rule to distinguish large-scale surface orientations from small-scale roughness on ice cliffs, since this is never totally clarified in other studies. The large-scale surface orientation is defined by a best fit plane with a diameter of 20 m. All irregularities smaller than these large-scale orientations are indicated as small-scale roughness.

The generated M3C2 distances are very sensitive to changes in the normal scale D (Lague et al., 2013). A normal scale equal or smaller than the small-scale surface roughness elements will result in scattered normal directions, which can be desirable when resulting distances are dependent upon small-

scale elements. In most cases however, geomorphological changes are not dependent upon these small-scale elements, but will only cause misdirected normals and significant distance overestimations. In these situations it is desirable to choose a normal scale equal or larger than the small-scale variations (see scale D_2 in Figure 1.3b) (Lague et al., 2013). However, a too large-scale is also not desirable, as this will neglect important large-scale orientations. This implies the urgency at finding a balance between these factors, which will result in an ideal normal scale.

Lague et al. (2013) developed an automatic approach to find this optimal normal scale for minimalizing the influence of small-scale roughness, but keeping larger scale orientations, by using a multiscale normal. The normal scale will iteratively change within a user-defined range and the scale in which the surface appears most planar will be chosen (Lague et al., 2013). Since the small-scale roughness on scale D and the large-scale orientations will be different in almost every location, the optimal normal scale also spatially fluctuates. Lague et al. (2013) found D_{opt} to be small in high curvature areas (like overhanging parts), small to intermediate on flat areas and large on debris-covered areas. This research does not provide details about the calculation of the multiscale normal (see Brodu & Lague (2012) and Lague et al. (2013)), since this technique is not suitable for this study (see section 3.2.3).

Besides a multiscale normal, the M3C2 algorithm also allows for constraining the normal orientation purely in horizontal direction. In this case, the normal can only fluctuate in the horizontal plane, while the vertical plane is fixed. This can be desirable when surface orientations can only alter the normal direction horizontally, i.e. the measured change is only dependent on the orientation within the horizontal direction. A last option is to erase all normal calculations and to only use the purely vertical direction (Girardeau-Montaut, 2015). This can be interpreted as the DoD technique on 3D point clouds.

1.5 Research aim

Brun et al. (2016) developed an alternative promising method to evaluate total cliff backwasting volumes. The cliff backwasting volume was obtained by measuring the volume sandwiched between the cliff outlines at t_1 and t_2. Subsequently, the backwasting distance was calculated by dividing the measured volume by the averaged t_1 and t_2 cliff area (Brun et al., 2016).

The backwasting rates as obtained from Brun et al. (2016) provide an accurate estimate of total volume losses and average cliff backwasting, which is already implemented in modelling validation (Buri et al., 2016b). However, also this study still could not reveal spatial patterns of ice cliff backwasting, as their method only allows for calculating an average effective backwasting rate. Spatial backwasting patterns can to this day only be calculated using distributed modelling studies (Buri et al., 2016a, 2016b). These distributed models are still computational very intensive, as they require a numerical interaction between the topography and atmospheric forcing.

This study therefore aims at providing a more direct and faster methodology to obtain distributed backwasting estimates than allowed by most recent modelling studies. The promising M3C2 algorithm requires testing of its capability in measuring ice cliff backwasting, as it could well provide a faster way to investigate melt patterns on ice cliffs. This possibly allows spatial upscaling of accurate melt estimates on ice cliffs, which could serve as an input for catchment scale hydrological models. Additionally, the backwasting patterns could further improve our understanding of the processes involved in ice cliff melt and the estimates can serve as valuable validation for ice cliff models, since distributed validation data is still not available (Brun et al., 2016). Therefore, this research addresses the following research question:

How can the M3C2 algorithm be used to directly quantify spatial backwasting patterns on ice cliffs on debris-covered glaciers and how can those observed patterns be explained?

In addition, the research aims to address four sub-questions:

1) What are the most promising settings of the M3C2 algorithm for calculating spatial backwasting patterns on ice cliffs according to experiments?
2) Which spatial backwasting patterns can be observed on the selected cliffs on the Langtang glacier and how can they be explained?
3) Can the approach be transferred to Lirung glacier and how do the results correspond to previously published results?
4) How significant is melt enhancement of ice cliffs, compared to the normal, flat debris-covered parts of the Langtang glacier?

The study starts with an overview of the study area, describing the most important properties of the Langtang catchment, glacier and the location of the selected ice cliffs. The methodology outlines the current issues for applying the M3C2 algorithm on ice cliff backwasting and the consequent design of the experiments. The results reveal the optimal M3C2 settings obtained from the experiments and the spatial backwasting patterns generated using these settings. The discussion will give an interpretation of the observed melting patterns, a comparison to other studies on another glacier and an overview of the research uncertainties. Finally, conclusions and recommendations for future research will be given.

2. Study area

The Langtang catchment (28°30'N, 85°30'E) is located in the Nepalese Himalaya, which is part of the Ganges basin (Figure 2.1) (Immerzeel et al., 2014; Immerzeel & Bierkens, 2012; Kraaijenbrink et al., 2016). The Ganges basin is characterized by a very high population. Almost 432 million people lived in this basin in 2000 and this number is projected to rise steeply towards the end of this century (Immerzeel & Bierkens, 2012). The meltwater contribution of the Ganges basin is estimated around only 10 %, which is low compared to other catchments in the Himalaya (Jianchu, Shrestha, & Eriksson, 2009). The area of the Langtang catchment is around 585 km^2 (Pellicciotti et al., 2015). The easterly winds during the monsoon season (June to September) bring on average 800 mm a^{-1}, which constitutes 70 % of the annual precipitation (Immerzeel, van Beek, Konz, Shrestha, & Bierkens, 2012). The catchment can therefore be classified as glacial, with high precipitation during the summer monsoon and very limited precipitation during the dry winter season (November to May). Average daily temperatures between 1957 to 2000 in the Langtang catchment has been measured on 0.5 °C during the winter season, while a much higher mean daily temperature of 8.4 °C has been measured during the summer months (Immerzeel et al., 2012).

The Langtang glacier is located approximately 100 km north of Kathmandu. The size of the glacier is approximately 59 km^2 and it is therefore the largest glacier in the upper Langtang catchment (Ragettli et al., 2016). The Langtang glacier is fed by four confluences with smaller tributary glaciers at approximately 1.5, 8.0, 12.0 and 13.5 km from the terminus and additionally by avalanches originating from the steep slopes besides the glacier (Kraaijenbrink et al., 2016). The accumulation area starts right below the steep slopes of the Langtang Peak (7200 m above sea level (asl)), having debris-free ice until 5200 m asl. From 5200 m to the glacier outlet on 4500 m asl, the glacier is characterized by a debris mantle, which represents 47 % of the glacier area (Tangborn & Rana, 2000). The debris thickness on the glacier is unknown, since measurements are lacking. The debris layer is assumed to be comparable with the Lirung glacier, which contains a thick (>60 cm), but highly variable (fine silt to large boulders) debris cover (Pellicciotti et al., 2015). The glacier shows considerable thinning underneath the debris cover. This thinning accelerated last decades and resulted in a negative mean mass balance of -0.78± 0.1 m w.e. a^{-1} (2006-2015) for the debris-covered parts of the Langtang glacier (Ragettli et al., 2016). The velocity of the Langtang glacier has been estimated on 0 to 10 m a^{-1} for the lower reaches of the glacier, 20 to 30 m a^{-1} for the higher parts of the glacier and on average 5.9 m a^{-1} for the debris-covered part (Pellicciotti et al., 2015; Ragettli et al., 2016). Glacier meltwater leaving the terminus forms the start of the Langtang Khola River, which is the main river in the Langtang catchment and dissect the U-shaped Langtang valley (Immerzeel et al., 2012). The Langtang Khola is an important tributary of the Trishuli River, which eventually drains towards the Ganges (Kraaijenbrink et al., 2016).

Many climate projections existing for the region emphasize the vulnerability of Himalayan glaciers to future climate change (Agrawala et al., 2003; Nakawo, 2009; Sharma, Moore, & Vorosmarty, 2000). For the Langtang catchment, precipitation is projected to increase by most General Circulation Models (GCM's) (Sharma et al., 2000). Also regional models project an increase in precipitation for this location, which is estimated on 1.9 mm a^{-1} (Immerzeel et al., 2012). The precipitation increases are most pronounced during the summer monsoon (Immerzeel et al., 2012). Because of a projected temperature rise of 0.06 °C a^{-1}, the glacier-specific yield of the Langtang glacier (i.e. melt rate per unit glacier area) will increase in future. The total glacier melt will also increase until at least 2050. Thereafter, the increasing glacier-specific yield cannot compensate anymore for the reduction in glacier area (Immerzeel et al., 2013). This will cause a peak in meltwater, which is projected to occur between 2045 and 2050 for the Langtang glacier (Immerzeel et al., 2013). The total discharge of this monsoon-driven catchment is very likely to increase towards the end of the century, because of an increase in precipitation and increasing glacier discharge until at least 2050 (Immerzeel et al., 2012, 2013). Immerzeel et al. (2012) estimated the discharge increase to be 4 mm a^{-1}. Small-scale projections for the Langtang catchment are

roughly in line with large-scale projections for the Ganges basin (Immerzeel et al., 2012; Lutz, Immerzeel, Shrestha, & Bierkens, 2014).
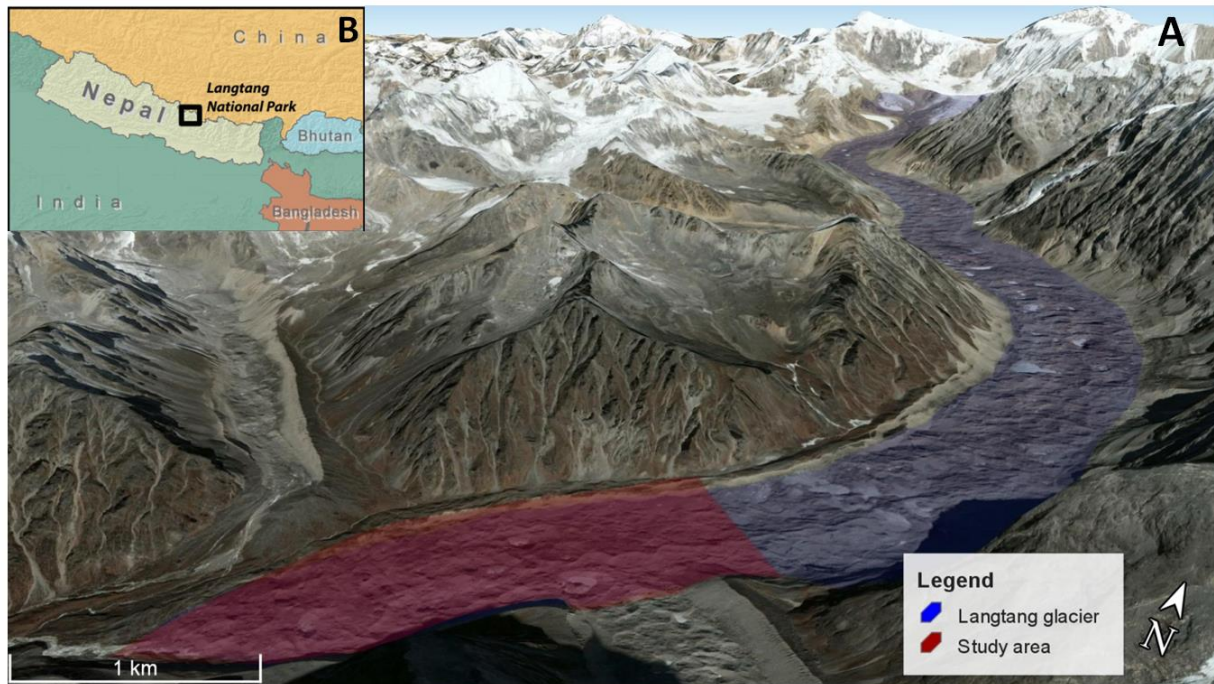

Figure 2.1 The Langtang glacier in blue (without its tributaries), monitored glacier area in red (A) and location of the Langtang National Park as illustrated by Kraaijenbrink et al. (2016) (B).

Glacial melt on the Langtang glacier is probably most significant at ice cliffs and around supraglacial ponds. 267 supraglacial ponds were detected on the entire Langtang glacier for May 2014, by using 5 m resolution RapidEye imagery (Kraaijenbrink et al., 2016). Kraaijenbrink et al. (2016) further identified 22 cliffs in May 2014 by adopting an object-based image analysis in an area near the glacier tongue, similar to the area analyzed in this study (Figure 2.2). The cliffs are characterized by a steep slope (between 35.2 and 77.2 ° with a mean of 44.6 °) and are therefore not covered by a thick debris layer (Kraaijenbrink et al., 2016). The cliffs are predominantly (14 out of 22) located on the south-eastern lateral half of the glacier tongue. The cliffs differ in shapes and characteristics. Some cliffs are more straight (e.g. cliff 7, 11 and 16), while others are more curved (e.g. cliff 13 and 12). Most of the cliffs (14 out of 22) are accompanied by supraglacial ponds and some cliffs tend to form circular systems around these ponds (cliff 13, 17 and 18) (Kraaijenbrink et al., 2016).

This study will stick to the cliff numbering as used in Kraaijenbrink et al. (2016). Cliff-pond system 7, 13 and 15 were selected for this research and their spatial backwasting patterns were analyzed. Cliff-pond system 15 consists of three separate cliffs in 2015 (15A, 15B and 15C). The cliff properties will be described in section 4.3 of the results. Appendix 1 provides 3D-illustrations of all studied cliff systems, combined with a visualization of their aspects.

No earlier studies have measured ablation of ice cliffs on the Langtang glacier specifically. Most modelling studies that aim at quantifying ice cliff backwasting focused on a UAV-monitored part of the smaller Lirung glacier (blue area, Figure 2.3). To compare the results of this study to other studies, one additional cliff (cliff 2) will be studied on this part of the Lirung glacier. The glacier is located approximately 13 km west of the Langtang glacier.
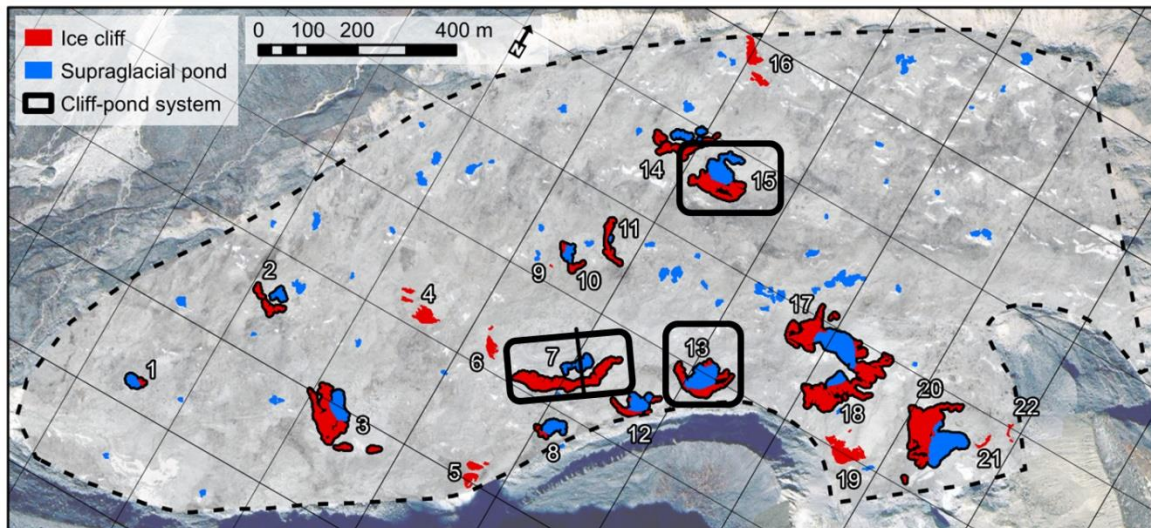
Figure 2.2 Cliff and supraglacial pond outline as identified by Kraaijenbrink et al. (2016). The cliffs in the boxes (7, 13 and 15) are selected for this research.
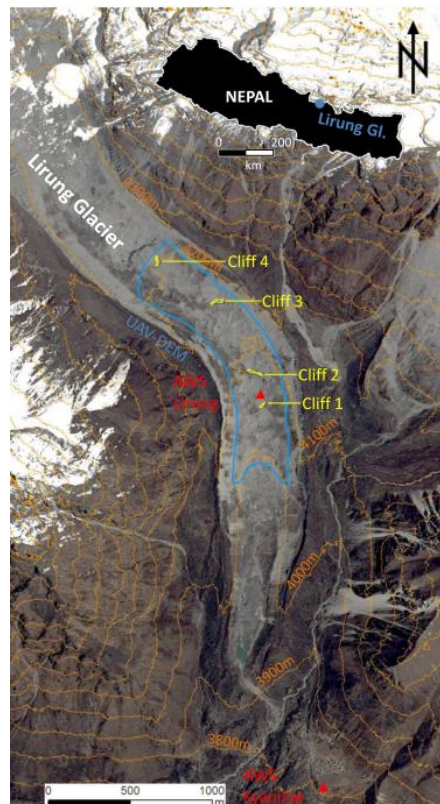

Figure 2.3 Location of the Lirung glacier and ice cliffs 1, 2, 3 and 4. Cliff 2 was used to compare results in this study to similar studies. The automatic weather stations AWS Lirung and Kyanjing are not relevant for this research (Buri et al., 2017).

3. Methodology

The 6 kilometer long snout of the Langtang glacier has been monitored by the Ebee drone (Sensefly, 2017) for multiple years (Immerzeel et al., 2014; Kraaijenbrink et al., 2016). The data is processed using the Structure for Motion (SfM) algorithms (Westoby, Brasington, Glasser, Hambrey, & Reynolds, 2012), as implemented in the software Agisoft Photoscan Professional version 1.1.6 (Agisoft LLC, 2014). Agisoft allows for the generation of a high-resolution point clouds from multiple overlapping images taken by a UAV (Immerzeel et al., 2014). A scale invariant feature transform (SIFT) was used to automatically detect and match characteristic features on at least two overlapping images, which is described by Lowe (2004). The sparse bundle adjustment system Bundler (Snavely, 2011) was consequently used to obtain the 3D camera orientations and positions, and to generate a sparse (i.e. low-density) point cloud (Immerzeel et al., 2014; Westoby et al., 2012). By applying multi-view stereo techniques (Westoby et al., 2012), a dense 3D point cloud was extracted. Ground control points (GCPs) and/or camera GPS locations were used to embed the output product into a coordinate system (Immerzeel et al., 2014; Kraaijenbrink et al., 2016). Elevation information from the point clouds were subsequently used to create orthomosaics and DEMs with a resolution of 0.1 m and 0.2 m, respectively. This study used high-resolution ($\pm$ 10 cm) point clouds of 7 May 2014 and 22 October 2015 and its products (DEM and orthomosaic) in the main analyses.

UAV surveys on 19 May and 22 October 2013 were used in many previous studies to estimate cliff backwasting from point clouds. This study used the same point clouds for estimating backwasting patterns to allow comparison. The point cloud generation followed the same workflow as described above.

The first step in this study is a DEM of differencing (DoD) analysis on the study area, in which the May 2014 DEM is subtracted from the October 2015 DEM. This could provide valuable information of melt rates on relatively horizontal areas of the glacier tongue and can moreover illustrate melt enhancement in cliff-pond systems. Secondly, the research will continue with experiments on the five selected cliffs to derive the optimal M3C2 settings for measuring ice cliff backwasting. Once these optimal settings are found, the resulting backwasting patterns for all cliffs will be outlined. These results include an additional backwasting pattern for cliff 2 on Lirung glacier that will be used only to compare the methodology to other studies conducted on the same cliff. Interpretations and possible explanations of the observed backwasting patterns on the Langtang glacier will be provided in the discussion section. Finally, the backwasting pattern of cliff 2 on the Lirung glacier will be compared to patterns found by modelling efforts and Brun et al. (2016). All these steps are illustrated in Figure 3.1.

3.1 DEM of difference (DoD) analysis

Although the DoD approach is not suitable to obtain reliable spatial backwasting patterns because of low information density on vertical parts, this method can be used to assess the vertical melt rate on flat areas of the glacier. It moreover illustrates the volumetric melt enhancement on ice cliffs. Two studies calculated elevation differences of the Langtang glacier using satellite remote sensing (Pellicciotti et al., 2015; Ragettli et al., 2016). However, the sensors used have a ground resolution that is often not high enough to identify individual features on the glacier. Therefore, Immerzeel et al. (2014) for the first time calculated elevation difference and glacial flow speed from high-resolution UAV point cloud data for the Lirung glacier. Such an analysis is still lacking for almost every other glacier in the Himalayas. Therefore, this DoD analysis aims at providing these high resolution glacier characteristics for the study area on the Langtang glacier.

The point clouds of May 2014 and October 2015 were imported in a GIS and were converted to DEMs with a resolution of 0.2 m. Large, clearly distinguishable boulders (n=115) were detected on both orthomosaics and the distance and arithmetic angle (direction) between these boulders was determined.

The distance data of these points were interpolated using ordinary kriging to create a displacement map. The flow direction and magnitude were further displayed using graduated arrows. These vectors, together with the flow speed map, provide an approximation of the non-uniform surface flow on the tongue of the Langtang glacier.

Using the flow speed and direction, the May 2014 DEM was transformed to exactly match the October 2015 location. The May 2014 DEM was subsequently subtracted from the October 2015 DEM to obtain a raster with elevation differences.
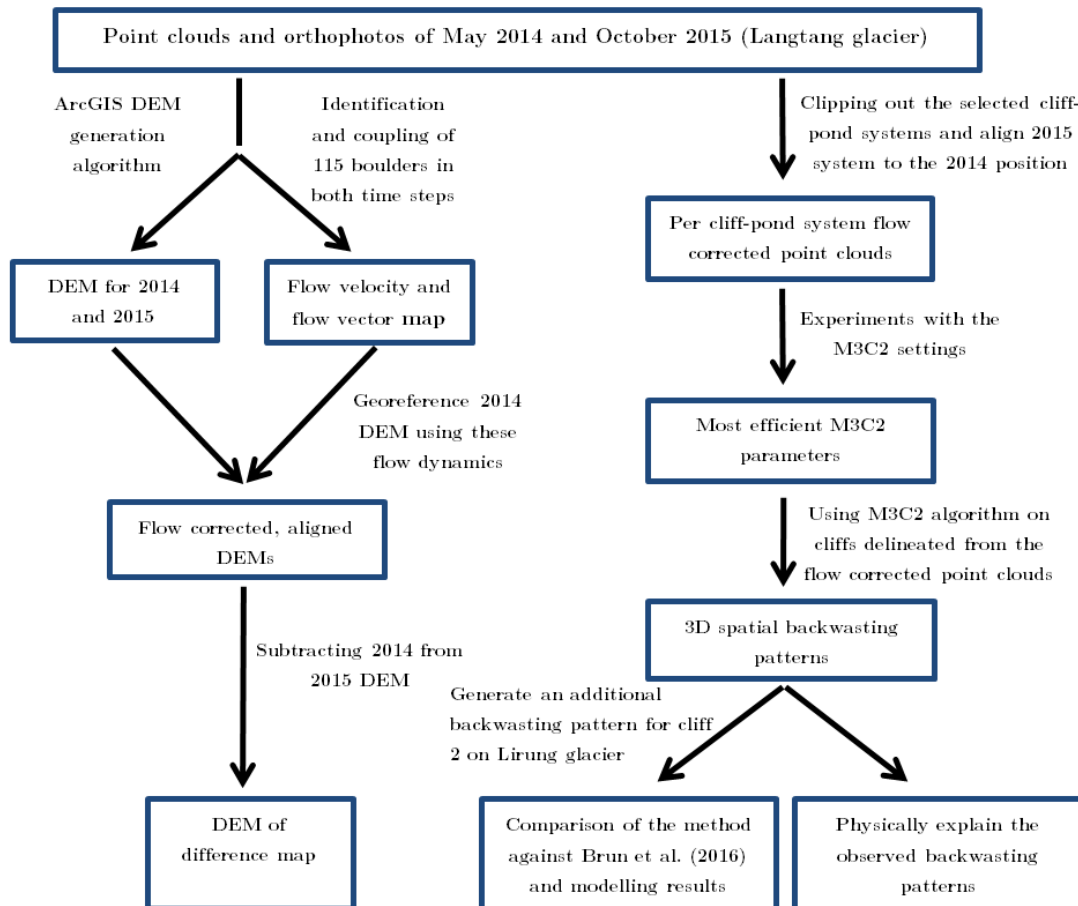

Figure 3.1 Flowchart illustrating the main research steps.

3.2 Extracting M3C2 cliff backwasting patterns

The DoD technique cannot provide reliable backwasting distances and 3D spatial backwasting patterns. Therefore, this part of the research aims to extract backwasting patterns by using the M3C2 algorithm. The M3C2 algorithm is implemented in the open-source software CloudCompare v. 2.6.2, which is the main software package used in this research (Girardeau-Montaut, 2015). The software is a point cloud and mesh editing and processing tool, which is primarily developed for direct change detection over two point clouds. The M3C2 algorithm is embedded in the software as an extra change detection plugin (Girardeau-Montaut, 2015).

The method used to derive the general cliff properties will be explained first, after which data preparation is presented. Finally, the ongoing issues in using the M3C2 algorithm are explained, as well as the design of experiments used to tackle these issues with respect to the determination of ice cliff backwasting.

3.2.1 Obtaining general cliff properties

Prior to all backwasting analyses in this research, the cliffs on Langtang glacier will be introduced by providing the main properties of the five different cliffs (area, slope, aspect, height and width) for 2014 and 2015. This was performed by analyzing the delineated cliffs (see 3.2.2 for the delineation method) in ArcMap 10.3.1 and CloudCompare 2.6.2. The (maximum) cliff height and width is manually measured on the point clouds by using CloudCompare. The cliff area was measured in the same software after constructing a mesh from the 3D point cloud. The slope and aspect were measured in ArcMap, by converting the point cloud to a raster. This raster was subsequently used for deriving per grid slope and aspect. By averaging these latter properties over all grid cells, the mean aspect and slope were derived. Mean aspect was calculated by converting the angles (in radians) to sin() and cos() prior to the mean calculation. Subsequently, the arctangent was calculated to estimate the mean angle (in radians), using the following formula:

$$\overline{\alpha} = atan2(\frac{1}{n} \cdot \sum_{j=1}^{n} \sin \alpha_j \, , \, \frac{1}{n} \cdot \sum_{j=1}^{n} \cos \alpha_j) \tag{2}$$

Where n = the sample size and α = angle in radians. As a final step, the average angle is converted to degrees to obtain the overall aspect of a cliff.

3.2.2 Point cloud preparation for a cliff backwasting analysis

M3C2 backwasting patterns must represent the effect of cliff backwasting only and a 3D correction for glacial movement (horizontal and emergence velocity) was therefore necessary. Each cliff-pond system (7, 13 and 15) on the Langtang glacier and its direct surroundings were individually delineated from the complete point cloud, which resulted in six point clouds (3 systems for both 2014 and 2015) as illustrated in appendix 1. The direct surroundings of the three cliff-pond systems in October 2015 were subsequently aligned to the May 2014 cliff-pond systems, by manually aligning at least 4 pairs of clearly identifiable boulders just besides the systems. The correction process was slightly different for cliff 2 on the Lirung glacier. To make the comparison to other studies more accurate, the same correction technique was applied. Brun et al. (2016) estimated the surface displacement around this cliff on 0.1, -0.8 and -1.0 m for Dx, Dy and Dz respectively, which was used to transform the May 2013 cliff to the position it would be in October 2013. After these corrections, the individual cliffs were subsequently delineated for both t_1 as t_2 to reduce calculation time and to avoid influence from other areas than these cliff areas (indicated by black lines in appendix 1, and appendix 2). The cliff areas were manually identified based on slope and colour of the surface, which was straightforward as they contain less debris and are generally steep. This correction for internal glacial movement and horizontal velocity and the cliff delineation process allowed for a detailed cliff backwasting study.

The definition of ice cliff backwasting in this study referred solely to the cliff locations where bare ice existed in both t_1 and t_2. Cliff parts that did get buried by debris between t_1 and t_2 or developed from the debris-covered glacier did not show continuous backwasting over the survey period. As the cliffs in cliff-pond system 15 present in October 2015 developed largely from more debris-covered surfaces (see Appendix 1, C), these patterns were not called cliff backwasting patterns, but cliff evolution patterns. Although the debris caused more uncertainty in the analysis, the evolution of these cliffs during their initial states still provided valuable information. For generating these patterns, only the cliff areas of October 2015 were delineated and consequently compared to the whole cliff-pond system as delineated earlier. Therefore, the data preparation for cliff 15 differed slightly from cliff 7 and 13.

3.2.3 Issues using M3C2 distances on ice cliff backwasting

The introduction outlined the possibilities of the complex M3C2 algorithm. An advantage of the M3C2 algorithm is that it does not require a priori information, since the normals determine the

measurement direction. However, Brun et al., (2016) stated that the M3C2 technique is not suitable for measuring ice cliff backwasting on the cliffs used in their study. Ice cliffs would not melt perpendicular to the cliff surface over the large time steps used in these studies. This resulted in a 82% loss of points for cliffs on the Lirung glacier (Brun et al., 2016). Even the multiscale normal developed by Lague et al. (2013) would generate much false directions for the measurements. This technique aims at decreasing the normal scales in high curvature areas (like cliff undercuts), while increasing the scale on relatively flat areas (Lague et al., 2013). This will result in even more missed normals than in case of choosing a randomly large normal scale, since the errors in high curvature areas will be very high. Therefore, also the multiscale normal will not work for measuring ice cliff backwasting. The use of normals for measuring ice cliff backwasting is therefore questionable.

Due to above mentioned reasoning and the findings of Brun et al. (2016), this study hypothesized that (1) the M3C2 algorithm with free surface normals at all normal scales will indeed result in a mismatch between the actual cliff backwasting direction and the direction of the surface normals, resulting in incorrect and incomplete distance values. (2) Constraining the normal direction using a priori information about cliff backwasting direction could considerably improve the results.

3.2.4 M3C2 experiments

A set of experiments were designed to enable testing of the above mentioned hypothesis. Both the projection scale (d) as the normal scale (D) are important user-defined parameters in the M3C2 algorithm. The normal scale (D) determines the radius around the core point for which points are selected to calculate the normal direction. After calculating the normal direction, the projection scale (d) determines the size of the cylinder used for the actual distance calculation along the normal direction. In these experiments, the projection scale (d) was constant on 1.5 m, since a change in this parameter will only change the amount of smoothing (averaging) of the distance calculation on the cliff surface. A scale of 1.5 m will not cause too much smoothing and will either not be too much influenced by outliers in the data at an average point spacing of 0.1 m.

However, the normal scale is a much more sensitive parameter as it can change the M3C2 distances significantly. The experiments therefore tested the influence of the normal scale on the calculated M3C2 distances. The M3C2 distances were calculated for each cliff from t_1 to t_2, using a certain normal scale. Subsequently, vertical cross-sections on each cliff (appendix 2) clipped a vertical profile from the generated backwasting pattern. Two scatterplots will be generated from each of these cross-sections (i.e. for each cliff), displaying for each point the calculated M3C2 distance on the x-axis and the vertical elevation on the y-axis.

The outcomes of the experiments were compared to expert judgement data. This expert judgement data was obtained by manually measuring and documenting the backwasting distance on certain elevations within the cross-sections.

Two sets of experiments were designed for this study, corresponding to the two parts of the hypothesis. The first set of experiments used the M3C2 algorithm with multiple unconstrained normal scales, meaning that the normals were not restricted in any direction and were purely determined by the cliff surface orientation within scale D. This will strengthen or attenuate the conclusion of Brun et al. (2016) that the M3C2 technique will result in an 82% loss of points because of unrealistic normal directions. The parameters will be a constant value of 1.5m for the projection scale and iteratively 1, 5, 20 and 50 m for the normal scale.

A second set of experiments was used to test if distances become more realistic when implementing an a priori constraint in the normal direction that is determined by the average backwasting direction of the ice cliff. An option provided within the M3C2 algorithm in CloudCompare enabled to constrain the normals in horizontal direction, which allowed only for fluctuations within the horizontal plane (i.e. from left to right). By rotating the delineated 2014 and 2015 ice cliffs (without resizing), the horizontal plane in which the normals are locked could be manually defined by the user.

This enabled to constrain the normals in a specific direction within the vertical plane, which is in the optimal situation equal to the average backwasting direction. Rotation of the cliffs was hereby an essential component, since the cliffs were not backwasting in a horizontal direction but were often lowering (compared to horizontal axis) on top of backwasting. As the backwasting direction differed for every individual ice cliff, the rotation process had to be repeated for every ice cliff studied. It is important to include the calculation of normal directions in the horizontal plane, as it allows for measuring cliff backwasting at curved cliffs, like cliff 15A. The experiment tested two different normal scales with a constraint in the horizontal plane: one fixed scale of 20 m (HNS20) and one cliff-dependent scale of a fourth of the width (HWD4). For the cliffs in this study, HNS20 is certainly large enough to erase small-scale roughness, but small enough to capture the large-scale orientation and cliff curvation within the horizontal plane. All other normal scales (1, 5 and 50 m) were therefore excluded prior to the second experiment. However, to enable this methodology on much larger cliffs than studied here (cliff 5 in Brun et al. (2016)) or much smaller cliffs (cliff 10 in Kraaijenbrink et al. (2016)), a normal scale dependent upon the cliff scale could be desirable. Small-scale roughness could become significantly larger on large cliffs and smaller on small cliffs. This could require a respectively larger or smaller normal scale (D) than 20 m to erase small-scale roughness and include large-scale orientations within the horizontal plane. Therefore, this experiment also tested the normal scale HWD4. This scale should for all cliffs be large enough to overcome small-scale roughness, but small enough to capture potential curving of the cliff within the horizontal plane.

These two experiments eventually revealed the most optimal settings for measuring cliff backwasting using the M3C2 algorithm.

The backwasting distance was always measured using normals calculated on the reference point cloud, based on the assumption of Lague et al. (2013) that many geomorphologic processes depend on the reference surface geometry. This also counts for melting on ice cliffs, since the initial geomorphology of the cliff influences the initial energy budget available for cliff melt. The observed cliff backwasting was therefore assumed to be more likely the result of the reference geometry, rather than the final one. This approach was confirmed by Buri et al. (2016b), who found that cliffs are melting perpendicular to the initial cliff surface using monthly time steps. Although the time step in this research is considerably larger, the assumption of perpendicular melt direction is much more corroborated on the initial cliff geometry rather than the final one.

3.2.5 Accuracy analysis

The point clouds and its products (DEMs and orthomosaics) were subjected to both horizontal and vertical errors. This section evaluates these errors based on the generated DEMs and orthomosaics, for the vertical and horizontal error respectively.

The point clouds used in this research were georeferenced using 16 Ground Control Points (GCPs) in May 2014 and 18 GCPs in October 2015, which were marked by $\pm$ 1 m² squares of bright red fabric. The UAV surveys of May 2014 and October 2015 were subjected to inaccuracies because of (1) the measurement errors of the Differential Global Positioning System (dGPS) base station and dGPS rover used to locate the GCPs and (2) output inaccuracies caused by the SfM processing technique.

The geodetic accuracy of the dGPS base station is reported on ~0.20 m for x, y and z (Wagnon et al., 2013). The dGPS rover was used to measure the exact location of the GCPs in a 30 seconds interval. The deviation between different measurements on the same GCP resulted in the input precision of the dGPS device, which was previously reported as very small (a couple of mm) (Immerzeel et al., 2014) and is therefore assumed to be negligible.

The SfM processing technique can cause additional errors, which can be evaluated by the horizontal and vertical errors at the GCP locations. However, since the image in this study is georeferenced using the GCPs, the errors can be higher further away from the GCPs.

Potentially large errors could be caused by displacement induced by the April 25 (Ghorka)

earthquake and its aftershocks. The displacement as measured by the dGPS base station on Lirung glacier (approximately 13 km from Langtang glacier) was -0.247, -1.256 and -0.754 m for respectively dX, dY and dZ. These displacements were also expected on the Langtang glacier, but can differ slightly because of the distance (approximately 13 km) between the glaciers. Directly measuring earthquake displacement using the Langtang dGPS base station was not possible.

The displacement on off-glacier terrain between t_1 and t_2 contains the sum of all errors described above. Therefore, this study calculated the horizontal and vertical error based on these off-glacier displacements. The horizontal and vertical displacement was calculated for stagnant locations on the lateral moraines of the glacier and variable areas (i.e. riverbeds or debris mounds induced by the earthquake) were therefore excluded from the analysis. 42 clearly identifiable boulders were linked using both the 2014 and 2015 orthomosaic, representing 42 point-pairs (Figure 3.2). The horizontal distance between these points was used to estimate the horizontal error. Elevation values on the point locations were extracted from 0.1 m resolution DEMs for both 2014 and 2015 and the elevation difference between linked points was subsequently used to calculate the vertical error. Both the horizontal and vertical errors were visualized in histograms.
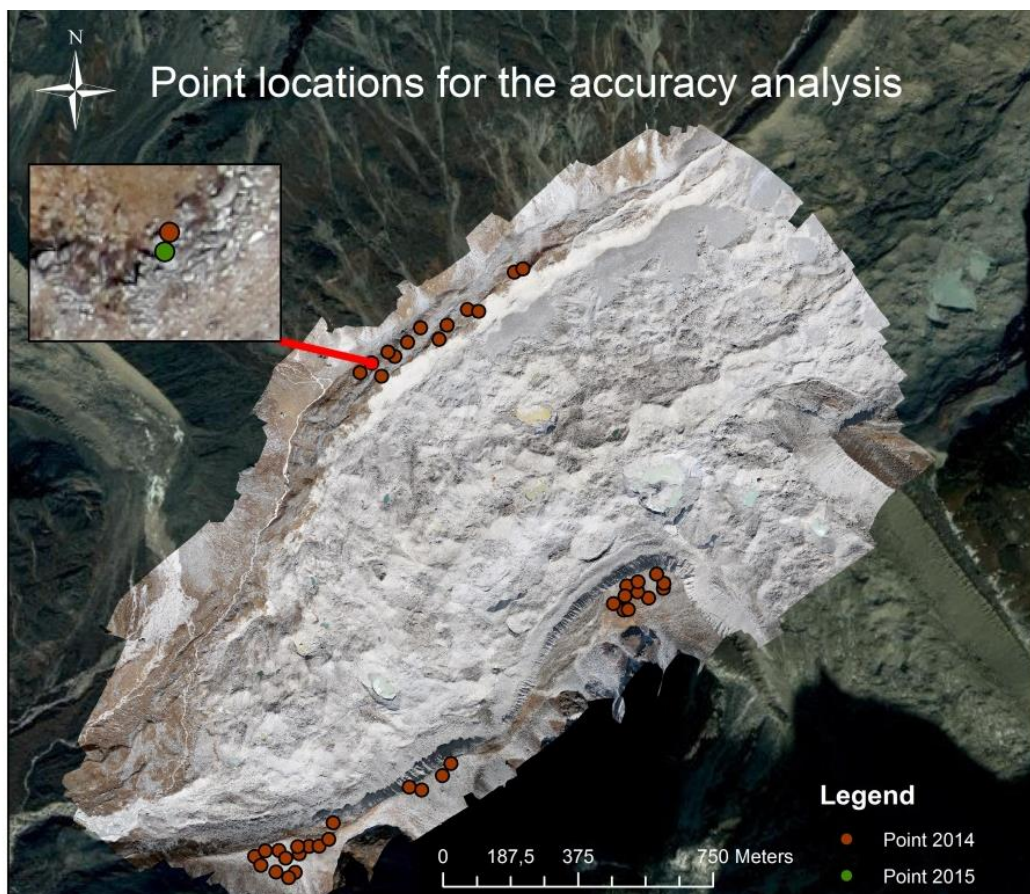

Figure 3.2 42 point-pairs that represents the same location in 2014 (red) and 2015 (green) as identified on the 2014 and 2015 orthomosaic.

4. Results

4.1 UAV data accuracy

The horizontal and the vertical errors on off-glacier terrain provide the summed error from the dGPS measurements, SfM algorithm and the Ghorka earthquake displacement. The mean of the horizontal error was 1.1 m with a standard deviation of 0.14 m (Figure 4.1, left). The horizontal errors were very consistent in both magnitude and direction. The vertical error was found to be -0.36 m on average with a standard deviation of 0.23 m (Figure 4.1, right).

These errors are higher than in previous studies using the exact same workflow. The accuracy of the dGPS base station was ~0.20 m for x, y and z. Kraaijenbrink et al. (2016) found an additional horizontal error of 0.05 m with a standard deviation of 0.04 m and a vertical error of 0.08 m with a standard deviation of 0.06 m on the GCPs, resulting from the SfM technique. Immerzeel et al. (2014) found most deviations at the GCPs to be less than 0.2 m for both the horizontal and vertical. These errors were very low, although these studies used the exact same workflow.

Therefore most of the displacement measured here must be caused by the earthquake, which was measured on 1.28 m and -0.754 m for the horizontal and vertical on the Lirung glacier. Assuming that the earthquake displacement was uniform over the study area, the average deviation from the mean displacement over all 42 points gives an indication of the dGPS and SfM processing errors. This deviation was 0.1 m in the horizontal and -0.18 m in the vertical and is in line with errors found by Kraaijenbrink et al. (2016) and Immerzeel et al. (2014) for the dGPS and SfM inaccuracies.

The total error was considerable for some analyses in this study. The horizontal error was directly embedded in the glacier-wide flow speed analysis. Since the error was roughly in line with the glacier flow direction, this caused a slight overestimation of the flow speed. The glacier-wide DEM differencing analysis was affected only by the vertical errors, since horizontal alignment did precede the analysis. However, the backwasting distances were not affected by these errors. The point clouds of the different cliff-pond systems were all aligned for both the vertical and horizontal prior to the M3C2 analyses.
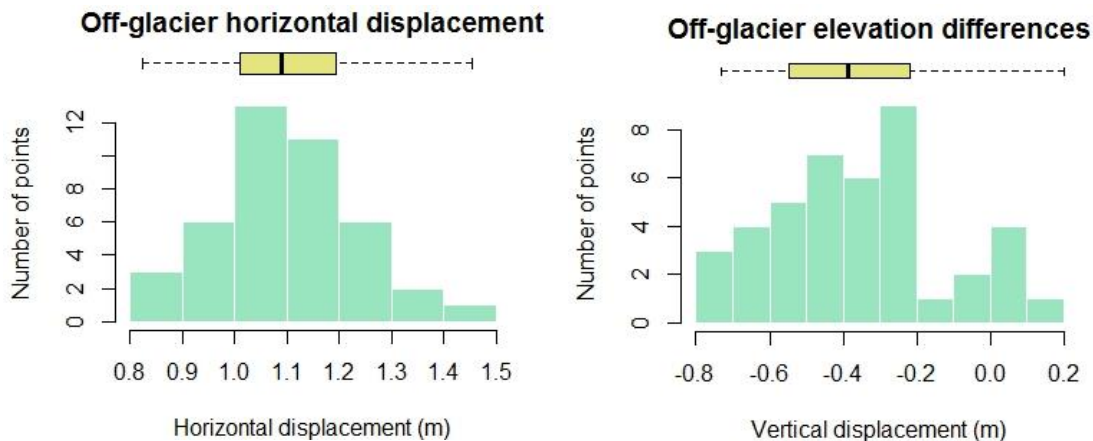

Figure 4.1 Histograms showing the horizontal displacement error (left) and the vertical elevation difference (right) as calculated from 42 point-pairs on different locations of the lateral moraines.

4.2 Elevation difference and glacier flow speed

The monitored part of the tongue of the Langtang glacier starts at an elevation of 4618 m and descends towards 4417 m with an irregular surface (Figure 4.3a). Subtraction of the May 2014 from the October 2015 DEM resulted in an average elevation difference of -1.1 m a^{-1} that ranged between 6.4 m a^{-1} and -16.5 m a^{-1} (Figure 4.3b). This elevation difference was slightly higher than the 2006-2015 ensemble mean of -0.91 ± 0.05 m a^{-1} found by Ragettli et al. (2016) for the debris-covered area on the Langtang glacier. This can be explained by the fact that the period in this study covers two monsoon seasons and only one winter season, which overestimated the annual elevation difference. The locations of cliff-pond systems did match almost perfectly with the locations of largest surface lowering. The relatively flat glacier areas showed an average surface lowering of -0.8 m a^{-1}, while the ice cliffs showed an elevation difference of around -10 to -16 m a^{-1}. This provided a clear indication of melt magnification on ice cliffs. The most prominent elevation increases corresponded to flat glacier areas right in front of large ice cliffs (as for cliff 7). This elevation increase is very remarkable, since the time step contains two ablation seasons and the flat glacier is hence subjected to much radiation. Its occurrence cannot be explained by present-day glaciological theories.

The surface displacement (Figure 4.3c) is on average 2.8 m a^{-1}, with maximum values around 4.8 m a^{-1} at the upper central section, and minimum, almost stagnant values of 0.7 m a^{-1} at the end of the tongue and near the glacier boundaries.

The masked areas (in black) belong to areas of very significant debris deposits, probably accumulated by debris-laden avalanches triggered by the Ghorka earthquake. Although these deposits were already large, most considerable depositions accumulated just upglacier of the study area as they were deposed by a much larger avalanche (Figure 4.2) (Ragettli et al., 2016). The debris depositions caused a sudden elevation increase of 1.33 m ± 0.42, which is very significant compared to the annual mean elevation difference of -0.55 m ± 0.13 between 2006-2015 on the Langtang glacier (Ragettli et al., 2016).
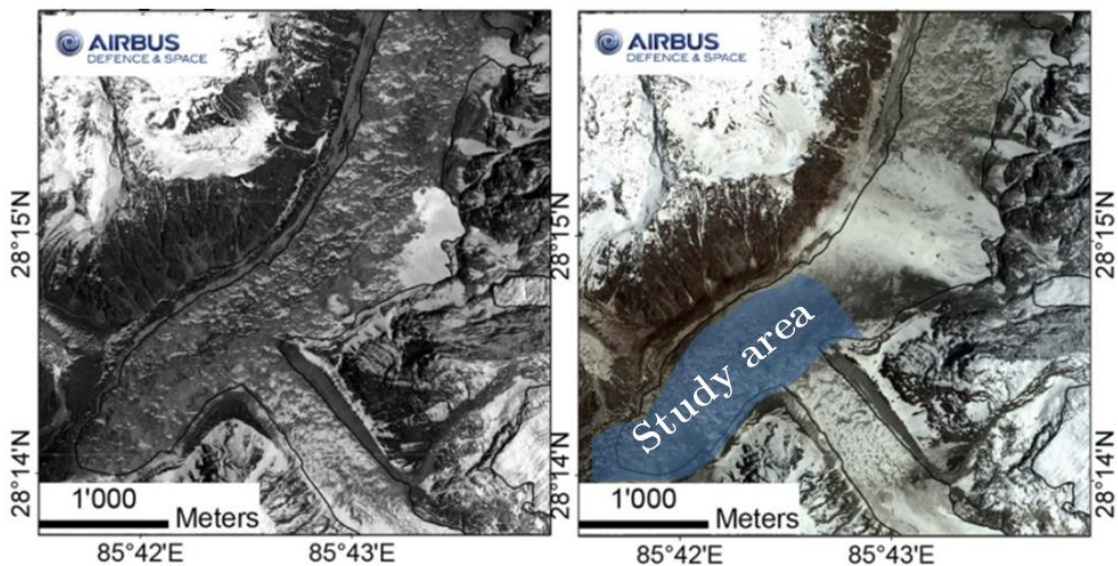

Figure 4.2 Satellite images illustrating the impact of the avalanche triggered by the Ghorka earthquake, before (April 2014, left) and after (May 2015, right) occurrence (Ragettli et al., 2016).
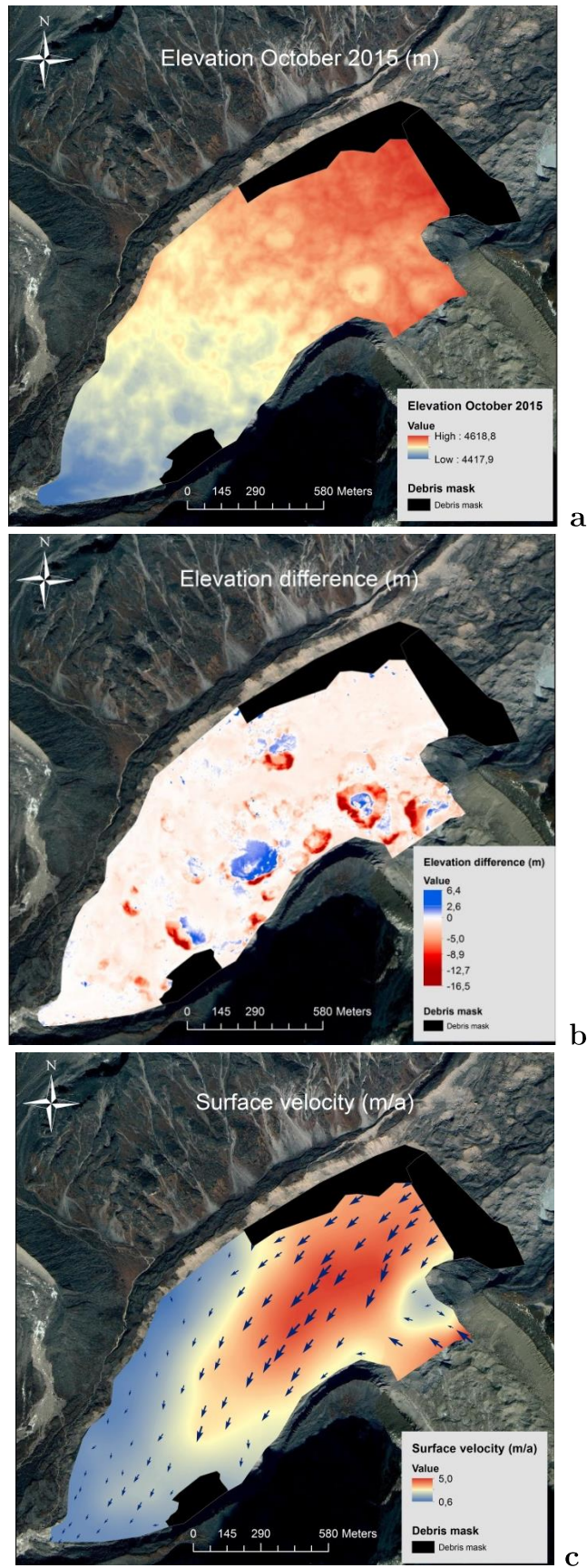
Figure 4.3 The 2015 DEM (a), the elevation difference between the 2014 and 2015 DEM (b) and the glacier flow velocity as derived from manual feature tracking (c).

4.3 General cliff properties

Cliff 7, 13, 15A, 15B and 15C were selected for measuring ice cliff backwasting on the Langtang glacier. These cliffs are suitable for this analysis as they are persistent over the surface period and they do not cause too much problems in the alignment due to non-uniform flow (as cliff 17). However, the cliffs all have a different geomorphology and size in May 2014 than in October 2015. In this section, a distinction between two different cliff types will be made, based on the studied cliff systems on the Langtang glacier. Cliff 13, cliff 15A, 15B and 15C will represent expanding cliffs, as they are expanding in both area and slope values. These properties decrease for cliff 7 that therefore represents reclining cliff systems with totally different dynamics.

4.3.1 Reclining cliff systems

Cliff 7 is the largest cliff system studied in this research (Table 4.1, Appendix 1 and Figure 4.4). With a slope of >49 ° this cliff was steeper than all other investigated cliffs and belongs to one of the steepest cliffs in the study area (Kraaijenbrink et al., 2016). In May 2014, the cliff area was 5512 m^2 and an undercut of around 883 m^2 was present at a part of the cliff (Kraaijenbrink et al., 2016). This undercut probably indicated the presence of a former supraglacial pond that disappeared before the survey. This also explains the rapid decline of the cliff area (to 1918 m^2 towards 2015) and slope after the pond drained. This decline could be an indication that the cliff is in its final stage, unless a new pond will form to sustain the cliff. Most of the cliff area has disappeared laterally at the most west-facing part of the cliff (blue area, Figure 4.4), reducing cliff width with almost 50 %. At this location, the cliff was already partly buried by debris in May 2014 and became completely buried towards October 2015. Some of the area decline was also attributed to a reduced cliff height of around 5 m at the persistent part of the cliff.
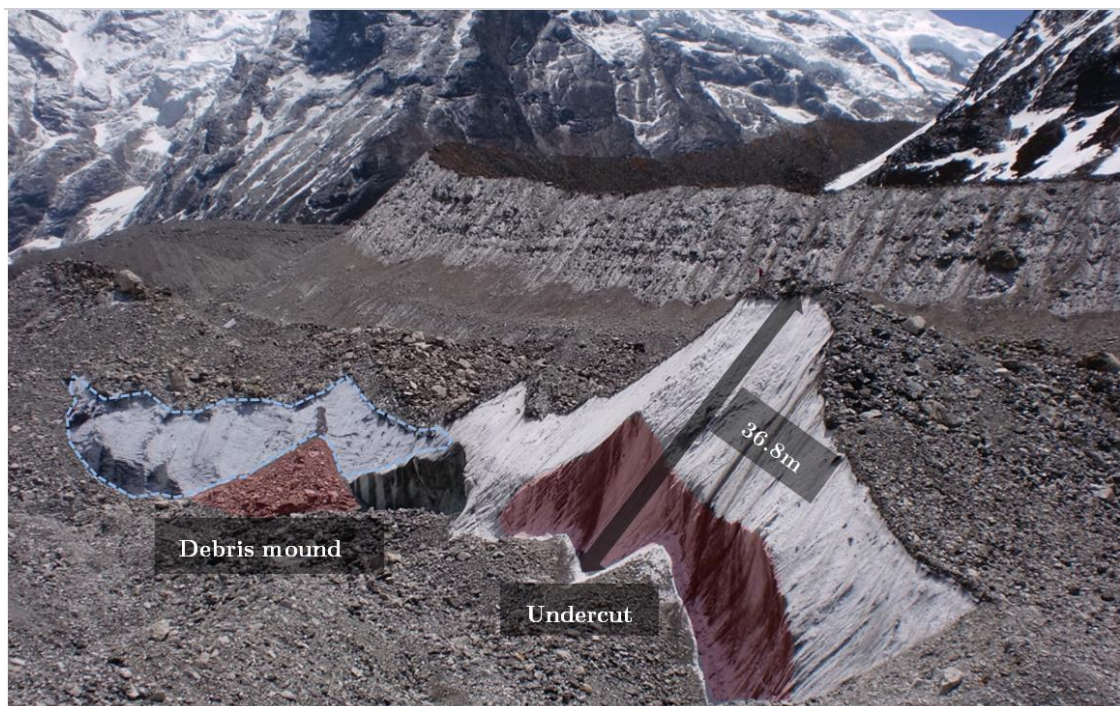

Figure 4.4 A photograph of the cliff which is referred to as cliff 7 (Photo credits © Pascal Buri and Evan Miles).

4.3.2 Expanding cliff systems

Cliff 13 is a relatively small, but a very rapidly lateral expanding cliff. The cliff area laterally expanded (to the right in appendix 1) from 775 m² in 2014 to 1824 m² in 2015, with a growth percentage of 135 % (Table 4.1). The cliff also steepened with a rate of 9 ° a⁻¹ and an overhanging part developed near the bottom of the cliff. Important for the melting dynamics of this ice cliff was the supraglacial pond present in May 2014, which had completely disappeared in October 2015. This pond stimulated the formation of the undercut and the lateral expansion of the cliff by enhanced melting at the subaqueous ice-pond interface.

Cliff-pond system 15 was divided into three parts for the October 2015 data (cliff 15A, 15B and 15C), since the three cliffs are all individual cliffs belonging to the same cliff-pond system. No easily identifiable cliffs were present in 2014, while above mentioned cliffs developed towards 2015. Cliff A and C were both relatively large (2034 m² and 1297 m², respectively) and steep, while cliff 15B was small (679 m²) and flatter (Table 4.1). These cliffs contained a total area of 4009 m² and formed during a period of 533 days including two ablation seasons. Cliff 15A faced west, 15C towards the (north)east and 15B was the most north-facing cliff of all cliffs investigated in this research. A supraglacial pond persisted between the UAV surveys and even grew in area, but the water level dropped approximately 6 m.

Table 4.1 Quantification of most important cliff properties, as measured in May 2014 and October 2015.

Cliff #	Cliff area (m²)		Cliff area change (%)	Aspect (°)		Slope (°)		Cliff width, height (m)	
	2014	2015		2014	2015	2014	2015	2014	2015
7	5512	1918	-65	322(NW)	333 (NW)	50	49	203, 37	114, 32
13	775	1824	135	316(NW)	321 (NW)	39	52	48, 16	100, 17
15A	-	2034	-	-	272 (W)	-	40	-	95, 25
15B	-	679	-	-	342 (NW)	-	38	-	22, 31
15C	-	1297	-	-	56 (NE)	-	42	-	40, 37

4.4 Cliff backwasting patterns

4.4.1 Outcomes of the experiments

The first experiment: using perpendicular surface normals

The first experiment aimed to confirm findings by Brun et al. (2016) that non-perpendicular melting of ice cliffs impeded the use of the M3C2 algorithm. The resulting scatterplots in Figure 4.5 provide an overview of the M3C2 distances as calculated with different perpendicular normal scales (D) that were not constrained in any direction.

A normal scale of 1 m clearly resulted in undesired scattering, because of small-scale surface roughness. This was most evident for cliff 7 and 15B. Although this scattering was reduced when using a larger scale of 20 m or 50 m, even these large-scales could not provide proper backwasting patterns. The estimation was not accurate (cliff 7, 15B and 15C) or totally misdirected (cliff 13 and 15A). Most normal misses using large normal scales were found on ice cliffs that were lowering (compared to the horizontal axis) on top of backwasting and/or had a relatively flat slope in May 2014 (as cliff 13 in Figure 4.6). Lowering of the ice cliffs is a result of both lowering of the cliff top and lowering of the cliff base that is enhanced by the presence of a supraglacial pond. For cliff 13, the missed normals represented 64 % of all

calculated normals using a normal scale of 20 m (Figure 4.6). These findings confirmed the statement of Brun et al. (2016) on the Lirung glacier that ice cliffs are not backwasting perpendicular to the cliff surface for the time intervals used in these studies, also when using large normal scales. Therefore, the use of perpendicular surface normals in the M3C2 algorithm to measure ice cliff backwasting was not appropriate.
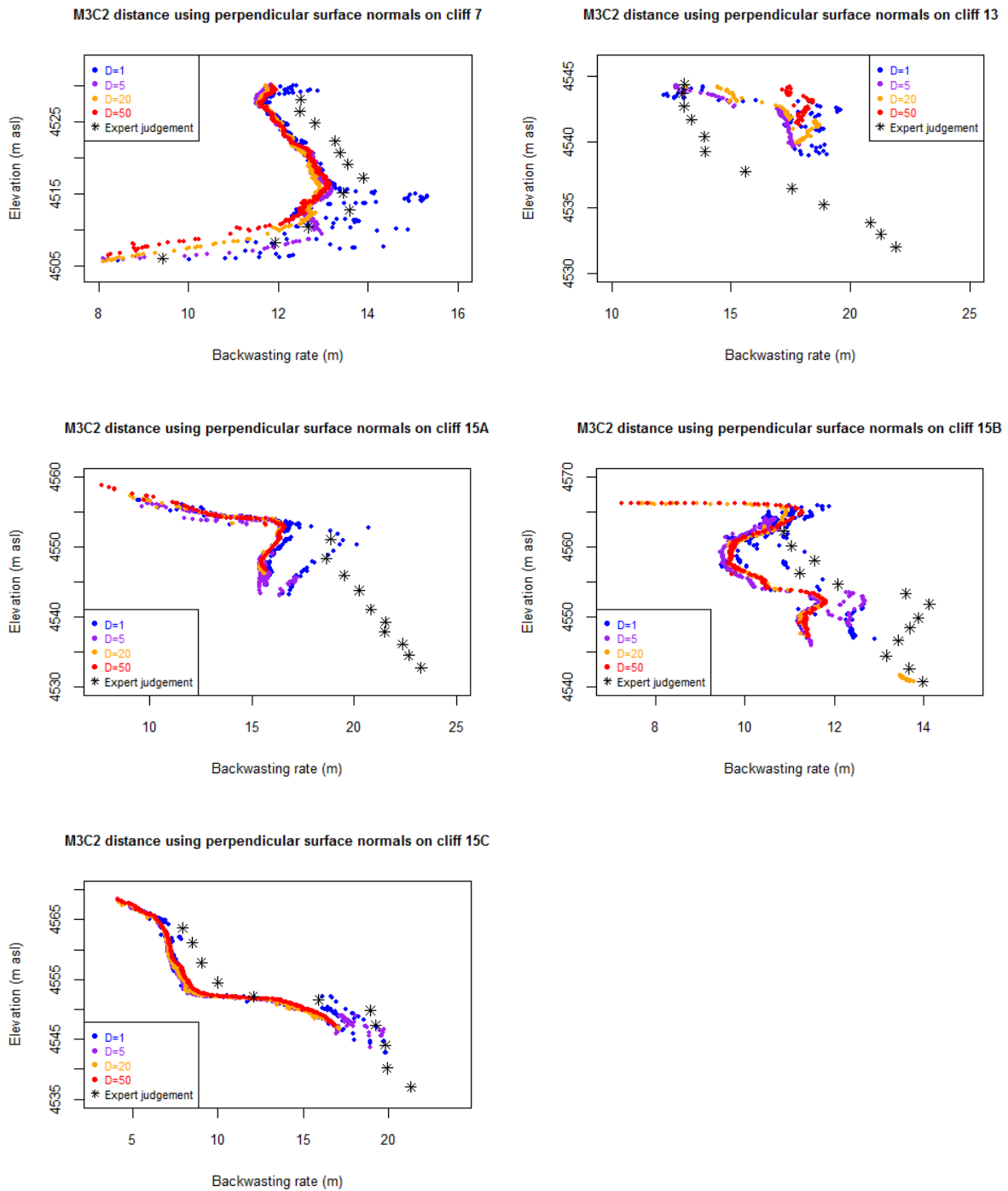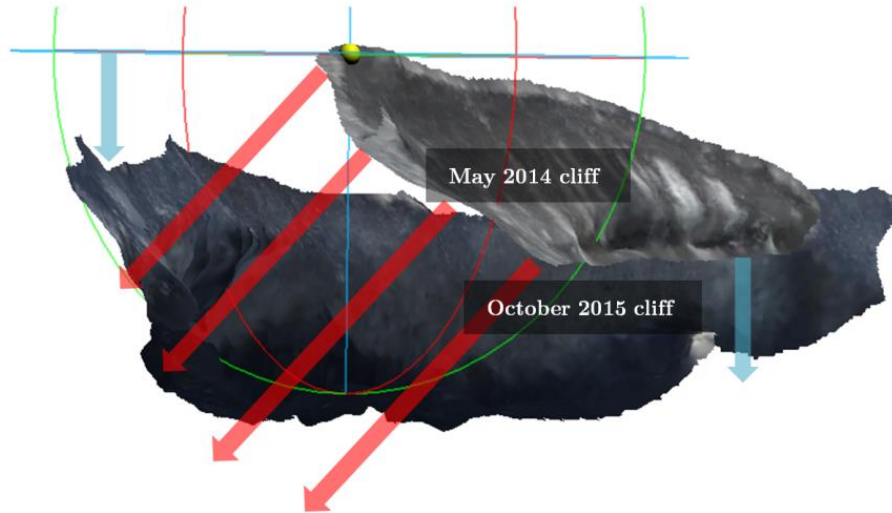

Figure 4.5 Backwasting distances calculated along perpendicular surface normals

Figure 4.6 An example of totally misdirected normals (64% misses) when calculated on the 2014 surface of cliff 13. This illustrates the loss of points using a large normal scale because of non-perpendicular cliff backwasting. The red arrows illustrate the approximate direction of the surface normals at a 20m normal scale and the cyan arrows the amount of cliff lowering observed for this ice cliff.

The second experiment: using horizontally constrained surface normals

After these observations, the experiments continued by testing the effect of using a priori information about the observed backwasting direction in constraining the normal orientation (second part of the hypothesis). The cliffs were rotated such that the horizontal direction is equal to the average backwasting direction. A constraint in this direction will considerably improve the information density and quality of the distance measurement, since the normals point parallel in backwasting direction (Figure 4.7).
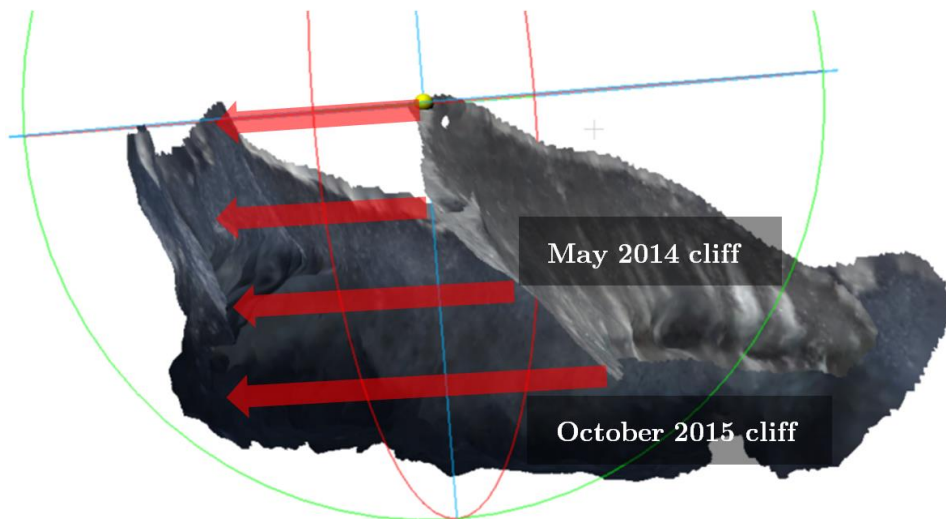

Figure 4.7 This figure illustrates the approximate direction of the surface normals after rotation and constrained within the horizontal plane.

The outcomes of the second set of experiments are shown in figure 4.8. The measured distances corresponded well with the expert judgements, which suggested that horizontally constrained normals are more accurate than free perpendicular surface normals. Especially for cliff 7, 13 and 15C the calculated distance was almost perfectly in line with the expert judgement analysis.

Both the scales HNS20 and HWD4 provided accurate backwasting patterns. However, HNS20 was most accurate as indicated by a slightly lower root-mean-square error (RMSE) (Table 4.2). HNS20 showed an average RMSE of 0.4 m, while HWD4 showed 0.5 m. Although the RMSE for cliff 7 was lower using HWD4, every other cliff gave better results for HNS20.
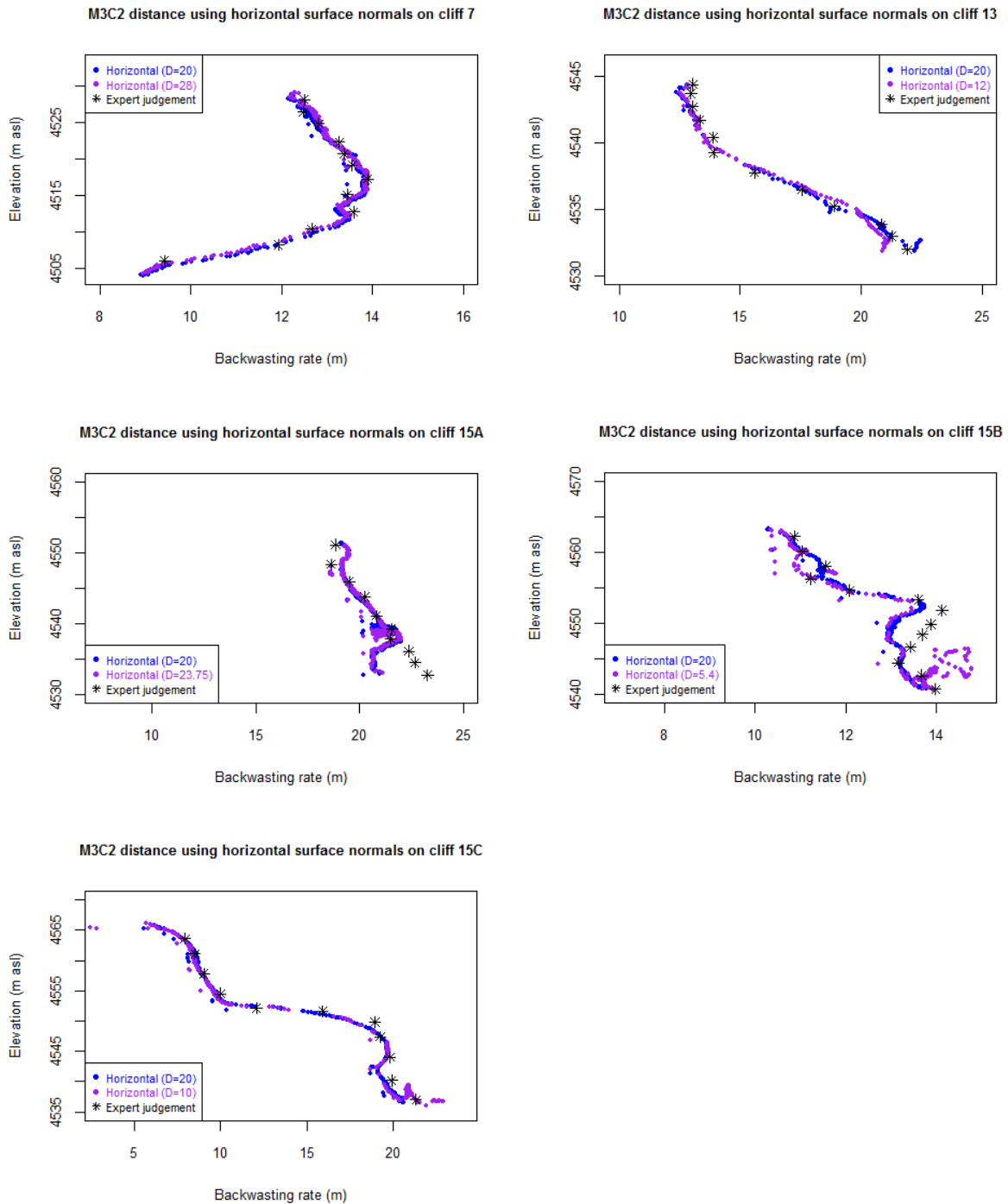

Figure 4.8 Backwasting distances calculated along constrained surface normals

Table 4.2 RMSE of the M3C2 distances calculated with horizontally constrained normals.

RMSE (m)		
Normal scale Cliff #	HNS20	HWD4
7	0.3	0.2
13	0.3	0.5
15A	0.7	0.9
15B	0.4	0.5
15C	0.2	0.4
Average over all cliffs	0.4	0.5

The RMSE of all experiments are summarized in Figure 4.9. The mean RMSE of using perpendicular surface normals was constantly >2 m for all normal scales, with a low change in RMSE when using different normal scales. Additionally, the amount of missed measurements was very high for all perpendicular normals, but this was not incorporated in the RMSE. Both small-scale as large-scale normals were therefore not suitable for measuring backwasting distance within the time step used here. The normal scales HNS20 and HWD4 provided much more accurate backwasting distances as their RMSE was both much lower than when using perpendicular normals. HNS20 was the most effective in generating accurate backwasting patterns for the cliffs selected in this study.
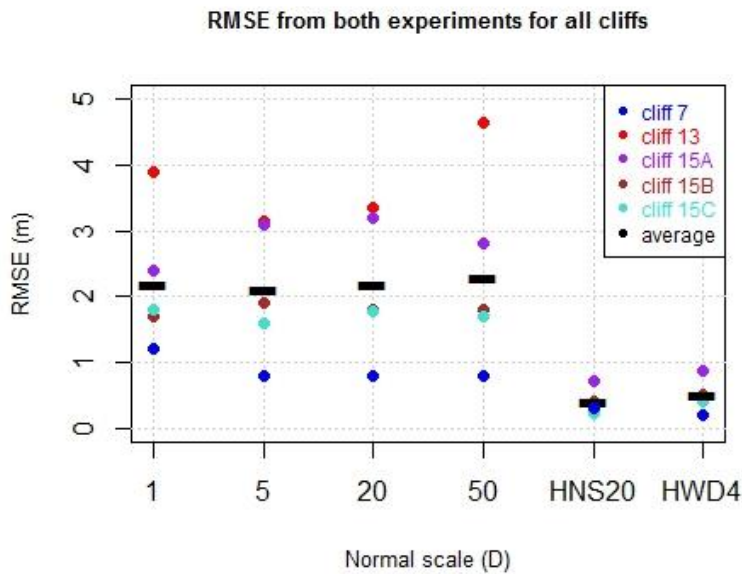

Figure 4.9 RMSE as calculated from both experiments and for all cliffs. The average per normal scale is indicated by the black lines.

4.4.2 Backwasting patterns on the selected cliffs

Backwasting patterns were generated for all cliffs selected in this study on the Langtang glacier (7, 13, 15A, 15B, 15C) using the M3C2 algorithm and a horizontally constrained normal scale of 20 m. These patterns show the amount of backwasting for the whole cliff area over the survey period of 533 days. To allow for comparison between results of this study and similar studies, the spatial backwasting pattern of cliff 2 on Lirung glacier will additionally be outlined.

A mean backwasting rate (MBR) was calculated for each cliff. This MBR was subsequently multiplied by the cliff area for which the M3C2 distances were calculated (corresponding to the smallest cliff area in t_1 or t_2) to obtain the backwasting volume. For all cliffs in cliff-pond system 15, the volume was calculated using the t_2 cliff areas only.

Cliff 7

The MBR of cliff 7 over the survey period is 15 m (i.e. 10.3 m a^{-1}) with a volumetric change of 28833.6 m³. The backwasting patterns found on this ice cliff fluctuated between a maximum of $\pm$ 19 m on the right side of the cliff and a minimum of $\pm$ 10 m in the undercut (Figure 4.10). Protruding areas of the 2014 cliff surface (indicated by area 1, 2 and 3) tended to melt much faster than depressions, like the undercut (area 4). This could possibly be explained by lower incoming radiation because of self-shading in these undercuts, especially at high solar zenith angles. For a large part of the undercut, backwasting distances were absent due to disappearance of the cliff towards 2015. Lower melting rates in the undercut probably caused slope relaxation and cliff burial by debris, which dropped from the glacier surface as the cliff melted.
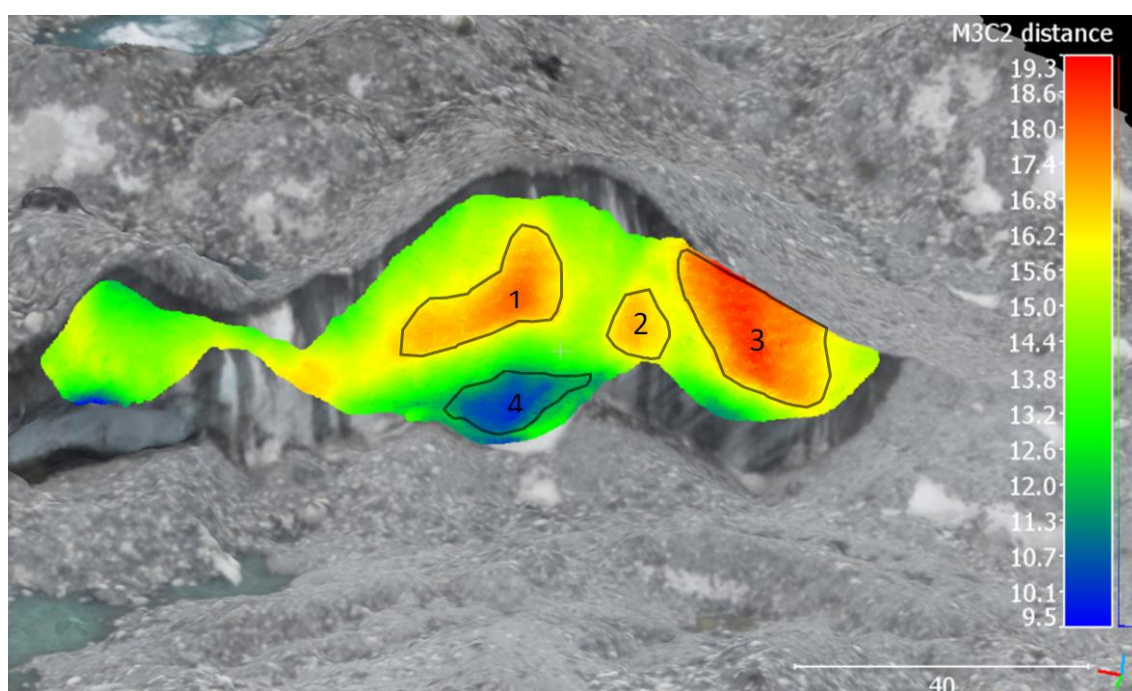

Figure 4.10 The backwasting pattern of cliff 7.

Cliff 13

Measuring cliff backwasting on cliff 13 was more difficult than for cliff 7, since backwasting was far less perpendicular and the surface geometry changed considerably over the survey period. Nevertheless, by using horizontally constrained normals, proper backwasting patterns could still be developed (Figure 4.11). The MBR was 17.8 m (i.e. 11.9 m a^{-1}), but exhibited large fluctuations over the surface. The volumetric change was estimated on 13831 m^3. The presence of a supraglacial pond accelerated backwasting at the cliff base towards $\pm$ 22-24 m and caused a negative melt gradient from base to top, resulting in relatively low backwasting values ($\pm$ 13 m) at the top left. The left side of the cliff showed overall lower backwasting rates than the right side of the cliff.
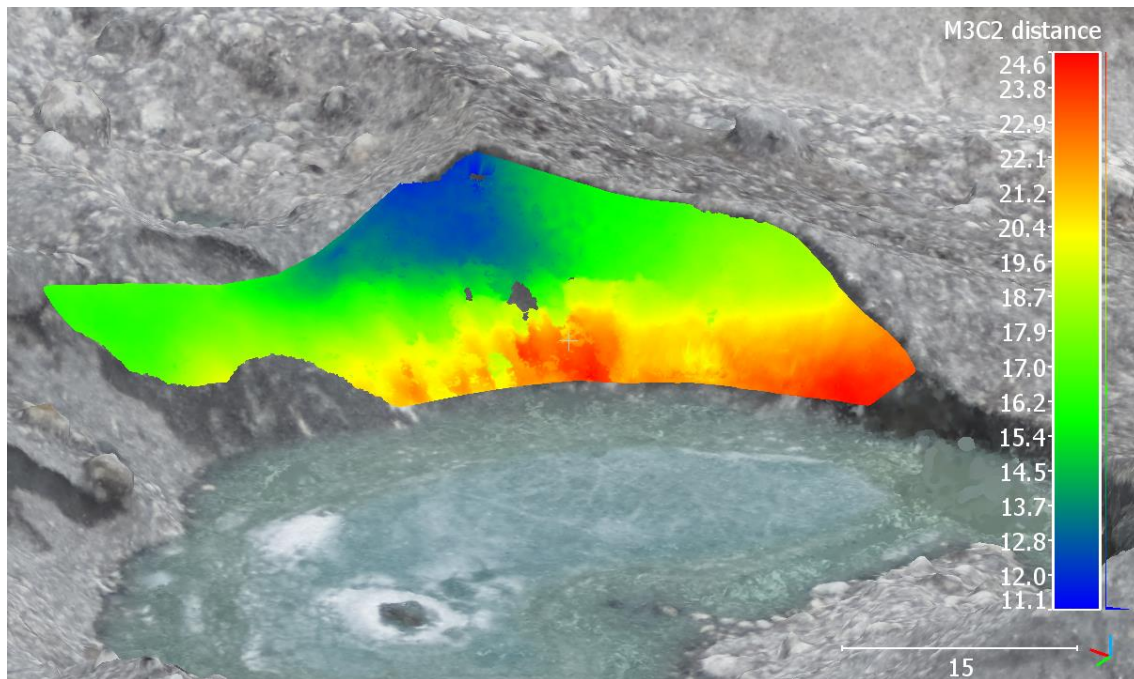

Figure 4.11 The backwasting pattern of cliff 13.

Cliff 15A, B and C

Before comparing all cliffs of cliff-pond system 15, evolution of all individual cliffs will be outlined.

Cliff 15A developed with a MBR of 18.2 m (i.e. 12.5 m a^{-1}) and an estimated volume loss of 37010 m^3 (Figure 4.12). The central section of the cliff developed fastest, with a rate of about 20 m over the survey period. The supraglacial pond again caused increased melt rates for decreased elevation. At the boundaries of the cliff evolution profile, the backwasting was reduced to $\pm$ 15 m.

Cliff 15B is small compared to all other cliffs and has a MBR of 11.6 m (i.e. 7.8 m a^{-1}). The volume loss is around 7908 m^3. Because of the presence of a supraglacial pond, this cliff also revealed increased backwasting for decreased elevation. Low backwasting values of around 9.5 m were observed on the top-left part of the cliff. Increased backwasting values of up to 14.3 m were found in area 1, but these were believed to be formed by erosion of a very large boulder that dropped down from location 'a' during cliff melt (Figure 4.13).
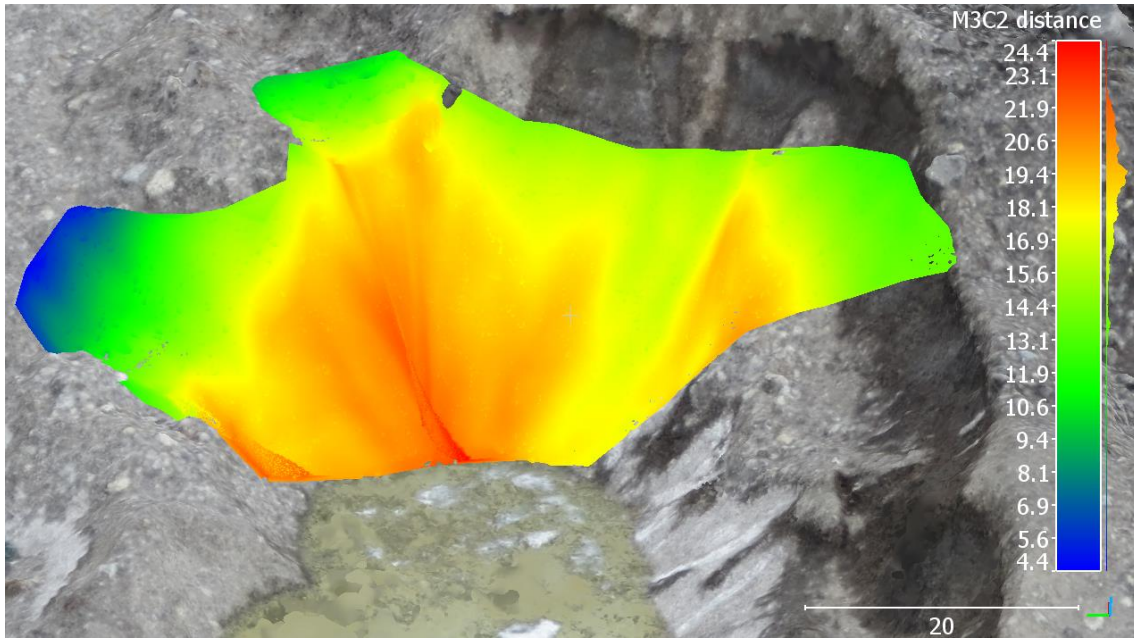
Figure 4.12 The evolution pattern for cliff 15A.

Cliff 15C was backwasting with a MBR of 14 m (9.4 m a⁻¹) and lost a volume of 18194.1 m³ (Figure 4.14). The cliff consists of two relatively steep parts (area 1 and 2) and one flat part in the middle section. Most backwasting was observed at the steeper base of the cliff (area 1), with values around 20-23 m. Above the cliff base melting rates were strongly reduced, with values between 10 and 3 m.
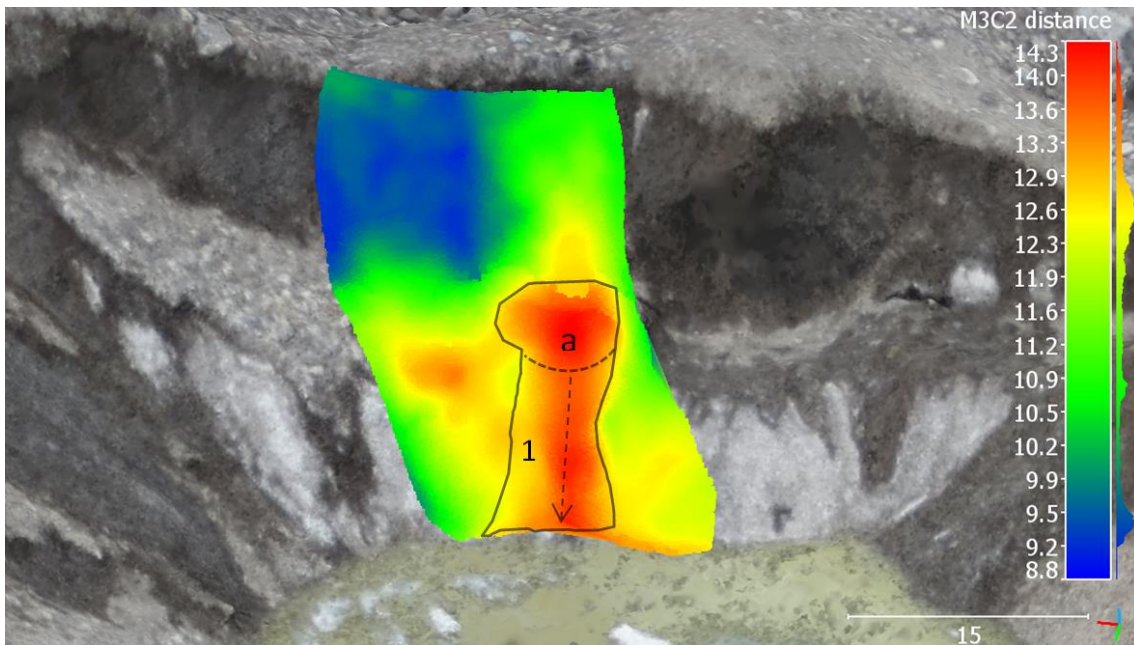

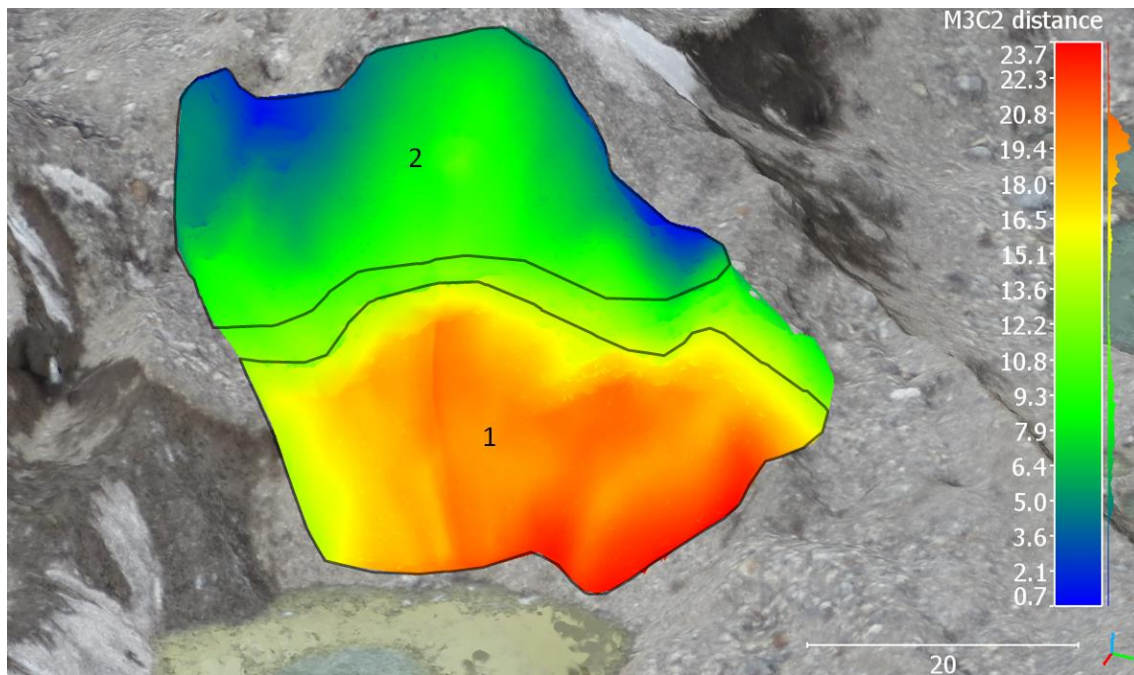**Figure 4.13** The evolution pattern for cliff 15B.

Figure 4.14 The evolution pattern for cliff 15C.

When comparing cliff 15A, 15B and 15C, interesting patterns could be observed (Figure 4.15). Cliff 15A developed significantly faster than the others, while cliff 15B developed slower. Although cliff 15A had a higher MBR than cliff 15C, the melt at the cliff base was approximately the same. However, melt at the 15B cliff base was very minor compared to the other cliffs.
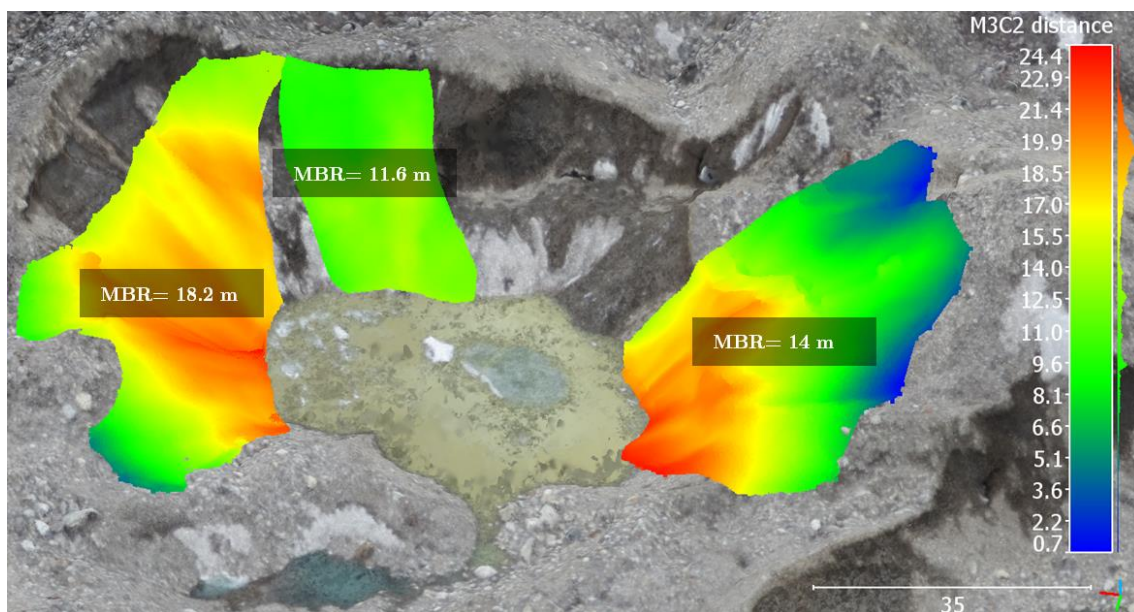

Figure 4.15 Cliff evolution patterns of all cliffs belonging to cliff-pond system 15.

Comparison between the cliffs

The cliff systems differed in MBR, with an average backwasting of 15.4 m over all cliffs (Table 4.3) that fluctuated between 11.6 m on the northwest-facing cliff 15B to 18.2 m for the west-facing cliff 15A (Table 4.3). Cliff 15A also generated the highest melt volume, as the cliff additionally consisted on a large area in 2015. Cliff 13 showed a higher MBR than cliff 7, but cliff 7 still generated more melt as the

36

cliff is considerably bigger than cliff 13. The variance of cliff melt fluctuated considerably among different cliffs. Cliff melt tended to increase with aspects further from the north(east) (Table 4.3).

Table 4.3 Overview of the backwasting measured on different cliff systems and their most important properties.

Cliff #	MBR (m)	Melt volume (m³)	Variance of backwasting	Pond presence	Average Slope (°)	Average aspect (°)
7	15	28834	3.4	No	49.4	327.7 (NW)
13	17.8	13831	9.1	Yes, in May 2014	45.1	318.8 (NW)
15A	18.2	37010	9	Yes, in both timesteps	40	271.6 (W)
15B	11.6	7908	2	Yes, in both timesteps	37.7	341.5 (NW)
15C	14	18194	33.8	Yes, in both timesteps	41.7	55.7 (NE)

Cliff 2 on Lirung glacier

Cliff 2 on the Lirung glacier was monitored by UAV on 19 May and 22 October 2013 (Buri et al., 2016b). Averaged over this period, the cliff was 21 m tall, 102 m wide and represented an area of 1921 m² (Brun et al., 2016). The cliff was persistent over the survey period, with remarkably few geometrical changes. A supraglacial pond was present in May, but completely drained towards October.

The MBR revealed to be 7.6 m over the survey period (Figure 4.16). The cumulative volume loss was calculated by multiplying with the same area as indicated by Brun et al. (2016) (1921m²), which resulted in a volume loss of $\pm$ 14600 m³. The spatial backwasting patterns revealed interesting dynamics. Cliff backwasting was relatively uniform over the entire cliff surface with a variance of only 0.8, which confirmed the uniform backwasting found by Buri et al. (2016b). The backwasting rates found in this study were highest on the base of the cliff adjacent to a small supraglacial pond (Figure 5.2, area 2). The top right and left of the cliff (area 1 and 3, respectively) also exhibited high backwasting rates, but they were lower than backwasting found at the cliff base. The enhanced melting at area 1 and 3 resulted in flattening of the October 2013 cliff surface at these locations, which was also reported by Buri et al. (2016b).
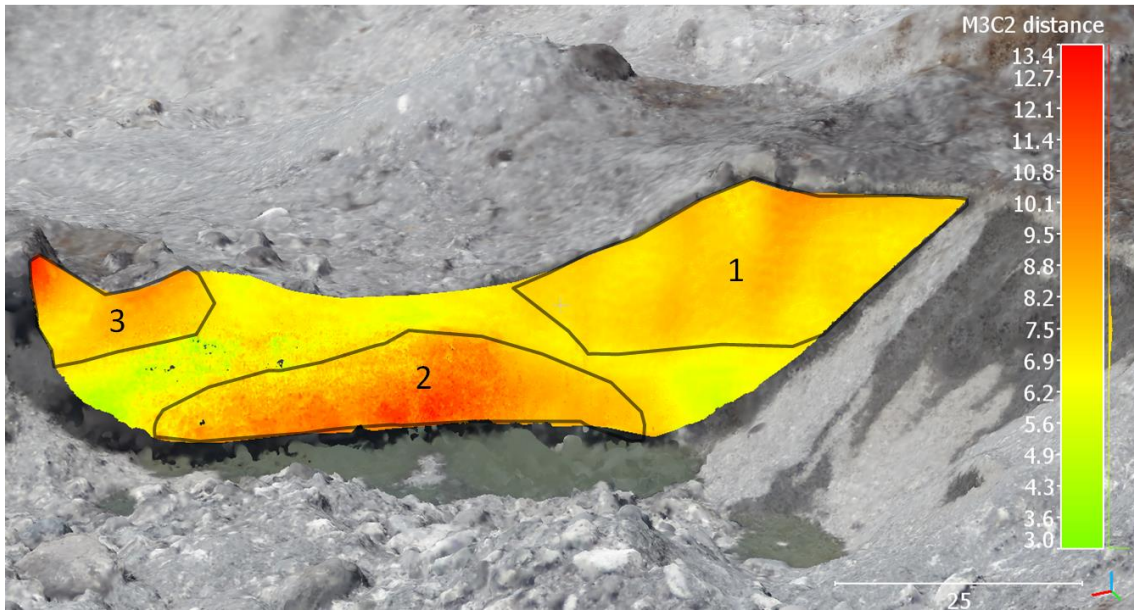
Figure 4.16 Spatial backwasting pattern for cliff 2 on Lirung glacier

5. Discussion

5.1 Causes for differences in backwasting patterns between ice cliffs

The five cliffs investigated on the Langtang glacier revealed variable mean backwasting, as well as heterogeneous backwasting patterns on the cliff surface. Although not physically modelled, these backwasting differences will be explained by (1) incoming shortwave radiation, (2) thermal erosion by ponds, (3) calving processes and (4) incoming longwave radiation from nearby debris mounds.

Aspect seems to be a controlling factor in the ablation and evolution of the studied ice cliffs. A trend of increased melt from north(eastern) aspects is observed for the studied cliffs (Table 4.3). Han et al. (2010) stated that south(west)-facing cliffs received more direct radiance than north(east)-facing cliffs, based on 38 cliffs on the Koxkar glacier in China and multiple studies suggested direct shortwave radiation to comprise a large part of the radiation balance (Buri et al., 2016a ; Han et al., 2010). The role of aspect in controlling melt rates is clearly visible on cliff 15B. Although this cliff is adjacent to a large pond that accelerated melting rates considerably at the neighboring cliffs 15A and 15C, the cliff showed the lowest backwasting rate of all cliffs in this research because of a very northern aspect. Besides a strong control on melt rates, aspect also controls cliff evolution. West-facing cliff sections disappeared for both cliff 7 as cliff 13, while cliff expansion or cliff persistence could be observed on their north-facing parts. This resulted in a mean aspect change towards the north for both cliffs and strengthens the hypothesis of the survival of north-facing cliffs by Sakai et al. (2002). So although north-facing cliffs showed lower ablation rates, they are more persistent than cliffs facing more southern.

Multiple studies stated supraglacial ponds as very important for the life-cycle of ice cliffs (e.g. Benn et al., 2012; Kraaijenbrink et al., 2016; Miles et al., 2016). Different observations in this study confirm the important role of supraglacial ponds in the evolution and ablation of ice cliffs. Considerable thermal erosion was observed for cliff 13, as indicated by the relatively high backwasting values at the cliff base. This thermal erosion could be measured because the pond was drained in the second UAV survey. The measurements from the 2014 cliff base could therefore point into the undercut present in the 2015 cliff. At cliff 7, the large west-facing section (blue area, Figure 4.4) was probably sustained by a supraglacial pond before May 2014 and disappeared during the survey period because the pond was drained. The rapid cliff development in cliff-pond system 15 is stimulated by thermal erosion from the large and persistent supraglacial pond located in the middle of the system. The water level dropped with around 6 meter, probably due to thermal erosion at the pond bottom and/or a slightly negative water balance of the pond. Large ponds often expand by calving ice from adjacent ice cliffs (Miles et al., 2016; Sakai et al., 2000). With a pond length of ± 80-90 m, this pond has enough fetch to intensify valley-wind driven water currents. These water currents are the factor process responsible for calving, as they considerably increase thermal erosion and therefore undercutting (Sakai et al., 2009). The high ablation and cliff formation rates in cliff-pond system 15 are therefore probably mainly caused by calving. The effect of calving may be visible in the melting pattern of cliff 15C, since the steep cliff base (area 1 in Figure 4.14) backwastes considerably faster than the rest of the cliff. It is hypothesized that this rapid backwasting resulted from calving of the steep cliff base after subaqueous ice melted underneath this section. Higher melt rates could be expected after calving of debris-covered parts, as the ice is clean and therefore more exposed to radiation. This could be the case in area 1 of cliff 15C that was covered by debris in 2014 (see Appendix 1, C) and probably evolved by calving. Also cliff 15A exhibits more backwasting near the cliff base, although this pattern is less evident than for cliff 15C. The more uniform slope of the 2014 surface could have caused more uniform calving over the cliff than observed for cliff 15C, which could explain why the vertical backwasting gradient on cliff 15A is less evident than on 15C. It is not clear from observations whether cliff 13 also melted by calving, but considered the smaller pond it is less likely.

Longwave radiation from debris is an important factor for the development of ice cliffs (Buri et al., 2016a ; Sakai et al., 2002). The contribution of longwave radiation was clearly less important or more

evenly distributed on the backwasting patterns than subaqueous melt and direct solar radiation, making it harder to detect. Cliff 13 showed higher backwasting patterns on the right side than on the left side, which cannot be explained by aspect or the supraglacial pond. These higher melting patterns could be caused by emissions of longwave radiation from a debris mound adjacent to the right side of the cliff (visible on lower right part of Figure 4.14). This could also explain the relatively low backwasting values on the left side of the cliff top.

These hypotheses about cliff evolution remain only speculative and could be strengthened by a similar study with smaller time steps between UAV surveys.

5.2 Comparison with other studies

Although modelling studies are still in their infancy, considerable progress was made last years. A sequence of model improvements was observed on cliff 1, 2, 3 and 4 of the Lirung glacier (Figure 2.3). The point-scale model of Steiner et al. (2015) modelled cliff backwasting on cliff 1 and 2. This model was improved by the first grid-based model of ice cliff ablation developed by Buri et al. (2016a). However, this model does not include sub-aqueous melt on the pond-ice interface, ice reburial by debris and does not allow for a dynamic update of the cliff geometry. A more recent study (Buri et al., 2016b) incorporated these processes in a dynamic grid-based numerical model. Brun et al. (2016) provided melt volumes and backwasting rates for the same cliffs of the Lirung glacier, which could be used for validation purposes. The volume sandwiched between the cliff outline in t_1 and t_2 was measured and divided by the mean cliff area of t_1 and t_2 to get backwasting rates averaged over an entire cliff. By averaging the modelled grid-based melt over an entire cliff, modelling results could be compared to Brun et al. (2016).

Above mentioned studies are compared to backwasting rates found in this study for cliff 2 on the Lirung glacier. The MBR for cliff 2 was converted to cm w.e. d^{-1} for comparison and is estimated on 4.36 cm w.e. d^{-1}. This value is similar to values derived from most recent studies (Table 5.1). A large difference is observed in the mean melt rate between the two distributed modelling studies by Buri et al. (2016a) and Buri et al. (2016b) that modelled 3.1 and 4.0 cm w.e. d^{-1} respectively. According to Brun et al. (2016), the lower value of 3.1 m is probably caused by neglecting the influence of radiative fluxes or thermal erosion from the supraglacial pond. The value is lower than estimated by Brun et al. (2016) and the records of ablation stakes over the period 8-20 May (Buri et al., 2016a). By incorporating the influence of the supraglacial pond at cliff 2 and allowing for a monthly update of the cliff geometry, Buri et al. (2016b) derived an almost equal, although slightly smaller, mean melt rate (4.0 cm w.e. d^{-1}) as derived using the M3C2 algorithm in this study (4.35 cm w.e. d^{-1}). This could indicate that the model estimate was improved. Brun et al. (2016) estimated the mean melt rate on 3.7 ± 0.74, which is lower than estimates in this study and the most recent modelling study of Buri et al. (2016b). However, the melt rates derived from Buri et al. (2016b) and this study falls just within the upper uncertainty margin (4.44 cm w.e. d^{-1}) of Brun et al. (2016). The proximity of these values to estimates in this study indicates that the M3C2 algorithm is an appropriate methodology for directly measuring ice cliff backwasting.

Table 5.1 Different mean melt rates (cm w.e. d^{-1}) on cliff 2 as found by multiple different studies

Study	Mean melt rate (cm w.e. d^{-1})
M3C2 distance	4.35
Steiner et al. (2015)	3.96
Buri et al. (2016a)	3.10
Buri et al. (2016b)	4.0
Brun et al. (2016)	3.70 (2.96-4.44)

The spatial backwasting pattern of cliff 2 was compared to melt patterns found by Buri et al. (2016a, 2016b). The spatial melting pattern of Buri et al. (2016a) used here results from the monsoon season (15 June- 19 September), which slightly differs from the period used in this study (19 May - 22 October). Since the melting patters of the pre-monsoon and post-monsoon season are similar to the monsoon season, the monsoon melting pattern can be used for a relative comparison of the patterns. Buri et al. (2016a) found higher melt rates at the upper half of the cliff, because of more incoming direct shortwave radiation (Figure 5.1, bottom). Longwave radiation from debris is highest at the edges of the cliff, both at the top and bottom, which causes increased melt at these locations. These spatial patterns do not perfectly correspond to patterns found in this study (Figure 5.1, top). The melt patterns on the western side of the cliff appear similar, since they increase slightly from bottom to top. In the middle and eastern section, almost opposite patterns were observed. This study suggests a strong pond influence that resulted in high backwasting rates around the middle of the cliff base. Buri et al. (2016a) did not incorporate the influence of ponds, which explains the contrasting pattern on this part of the cliff. Although incorporating an additional melt factor of 3.3 cm d^{-1} for subaqueous melt, also Buri et al. (2016b) underestimated enhanced melt by the pond. This can be derived from the vertical elevation profiles as they allow for a comparison between observed melt and modelled melt over different elevations in two cross-sections (Figure 5.2). The observed melt (blue to green line) is for both cross-sections slightly lower than the modelled melt (blue to red line) at the cliff top, while it is higher than modelled near the cliff bottom.
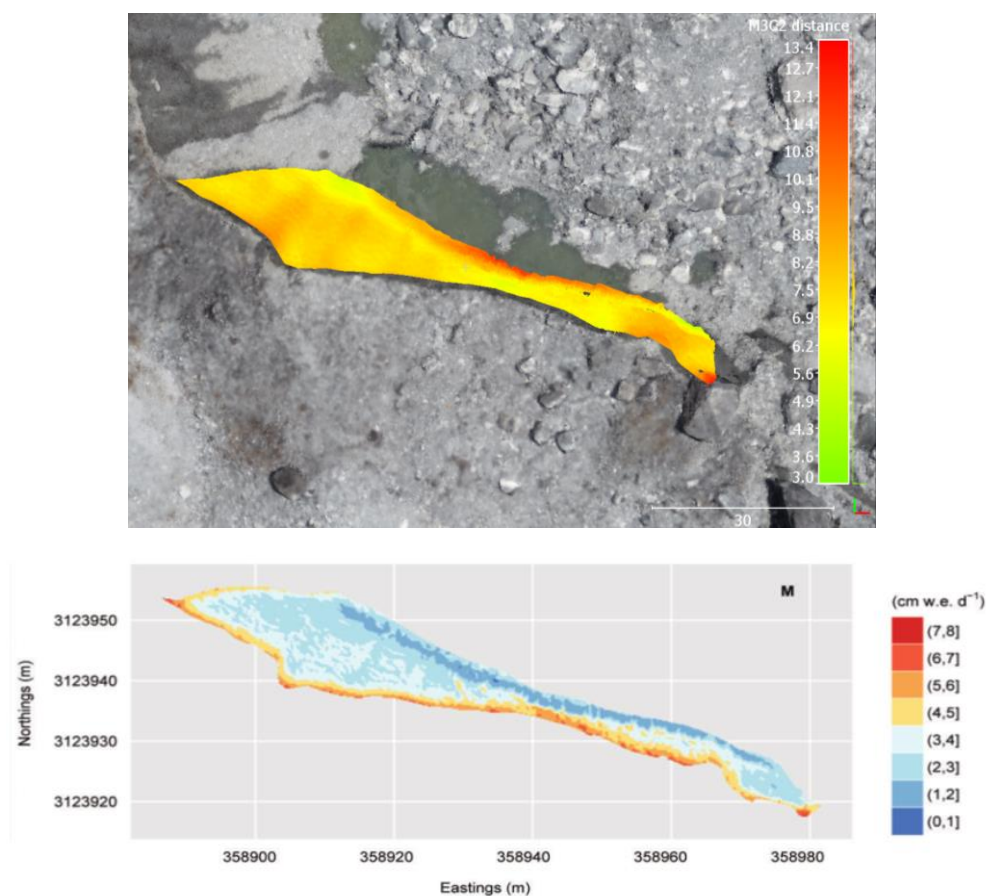

Figure 5.1 Top view on the M3C2 backwasting pattern (top) for allowing comparison with the melt pattern for the monsoon season as estimated by Buri et al. (2016a) (bottom).
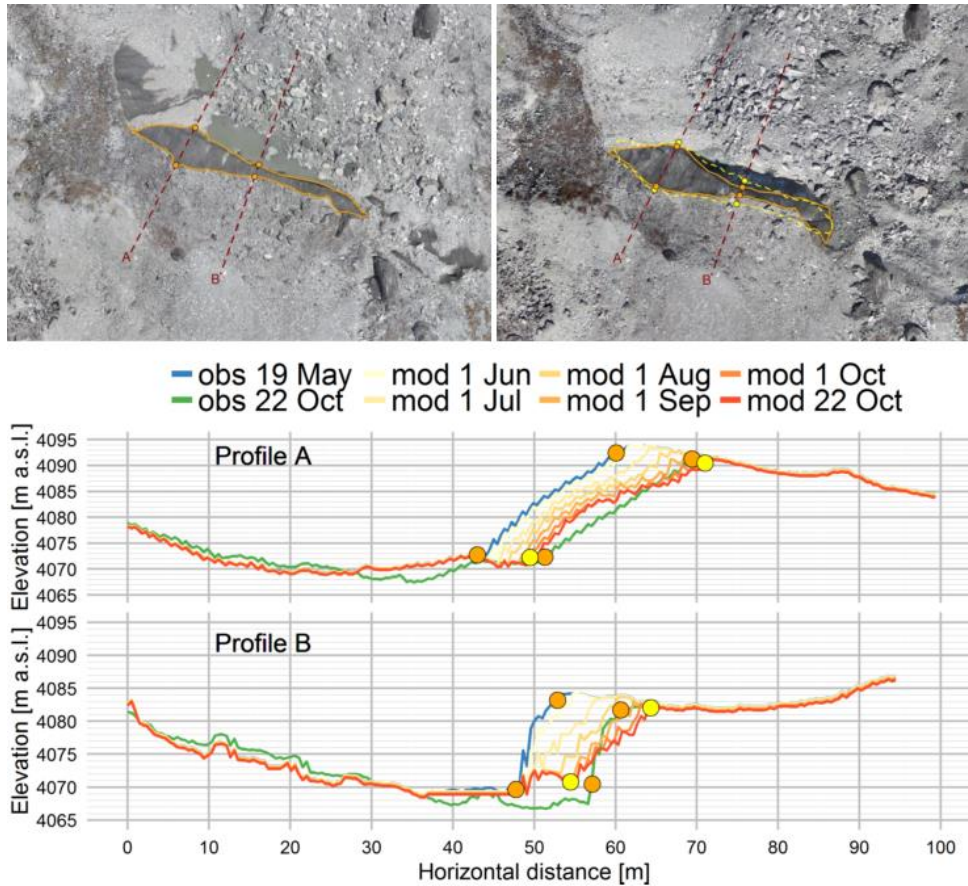
Figure 5.2 Top: Orthoimages showing the observed (orange) and modelled (yellow dashed) cliff outlines for May (left) and October 2013 (right). Bottom: Overview of the modelled melt from 19 May to 22 October (blue to red line) and the observed melt in the same period (blue to green line) over two cross-sections. The dots correspond to the debris-ice contact points for the observed (orange) and modelled (yellow) cliff (Buri et al., 2016b).

5.3 Uncertainties

Some limitations and uncertainties must be addressed in this research, especially for the data preparation, M3C2 measurement technique and for the large time step of 533 days.

Glacial alignment of the direct surroundings of ice cliffs in 2014 and 2015 was conducted to correct for the emergence and horizontal velocity of the glacier. However, these flat cliff surroundings did also melt vertically with about 1 m, which must inevitably be included in the alignment. This induces an extra error, since the ice cliff section in 2015 would in reality be located approximately 1 m lower than in the analysis. For an average backwasting rate of 15.4 m and assuming horizontal backwasting, this causes a slight distance underestimation in the order of 0.03 m. This underestimation can increase when ice cliffs exhibit increasing lowering on top of backwasting. Additionally, surroundings of cliff-pond systems never exhibited uniform flow direction and emergence, which result in a small RMSE after the alignment was done. Highly non-uniform flow around cliff 17 forced the exclusion of this cliff from the analysis.

The most efficient M3C2 settings were derived by comparing the backwasting patterns with an expert judgement over different cliff sections. The direction of the horizontal constraint in the M3C2 analysis is approximately equal to the measurement direction in the expert judgement, which stimulates their correspondence. Nevertheless, this correspondence shows that the normal scale of 20 m is large enough to accurately estimate directions within the horizontal plane.

The RMSE of HNS20 was only slightly lower than HWD4, but a normal scale dependent on cliff size could possibly be useful for much smaller or bigger cliffs than studied here. A scale of 20 will neglect cliff curvature on small cliffs and could potentially be too small to overcome roughness on very large cliffs. However, the normal scale of HWD4 could become so small for small cliffs that small-scale surface roughness starts to disturb the measurement direction. Small-scale roughness did not become smaller for the cliffs studied here, but rather caused undesired scattering of the surface normals. Cliffs in this research are too large to give a clear illustration of this effect, but the slightly higher RMSE obtained for HWD4 compared to HNS20 is believed to be caused by this process. If small-scale roughness does not become larger on very large cliffs, a normal scale of 20 m could also be accurate on cliffs much larger than investigated in this study. As radiation receipts on large cliffs can considerably fluctuate among different parts of the cliff, these cliffs can have high variabilities in large-scale cliff orientation (as cliff 5 in Brun et al. (2016)). The measurement directions are most accurate when they follow these large-scale orientations, but a large-scale normal of a fourth of the cliff width could well become too large for this purpose. Therefore, the HNS20 setting should also be able to generate backwasting patterns for cliffs much larger or smaller than studied here.

In the most recent modelling study of Buri et al. (2016b), ice cliffs were assumed to melt perpendicular to the cliff surface in a monthly time step. By forcing the cliff with incoming radiation fluxes, the model could reproduce cliff melt quite accurately. However, the melt direction over 533 days in this study is not anymore perpendicular to the cliff surface, which resulted in a high RMSE over all unconstrained normal experiments. The best measuring direction was therefore assumed to be the average backwasting direction of the cliff, which corresponds to the average top-to-top and bottom-to-bottom direction of the segmented cliff surfaces. This direction will result in the least distance measurement misses from t_1 to t_2, but is not necessarily equal to the real melt direction of a certain point on the cliff and to the melt that could be expected from the radiation balance. The most efficient horizontal direction to measure backwasting (i.e. average backwasting direction) can be altered over time by the shape of the flat glacier surface just behind the cliff (this can lower or increase elevation of the cliff top) or by downwasting of the cliff bottom because of the presence of a supraglacial pond. This could alter the measured backwasting distance, but has no direct relationship with changes in the incoming radiation on the cliff surface. The M3C2 backwasting rates can hence differ slightly from backwasting expected using the radiation balance in distributed modelling studies.

In the introduction, the DoD technique was stated as unsuitable for measuring ice cliff backwasting, since the information density at vertical parts of the cliff is very low. However, this technique could be useful after rotating the cliff for t_1 and t_2 so that the vertically oriented cliff becomes horizontal (e.g. Rosser, Petley, Lim, Dunning, & Allison, 2005). This could increase information density on ice cliffs and could create backwasting patterns of the same form as in this research. However, a disadvantage of this technique is that the direction is just vertically and normals cannot anymore be used to estimate the direction perpendicular to the surface in the vertical plane (which is the horizontal plane in this research). Especially at more curved cliffs (e.g. cliff 15A), this would result in a considerable increase in normals calculated on t_1 who miss the surface of t_2.

A smaller time step between the two surveys (e.g. six months, between May and October) would have been more efficient for the generation of backwasting patterns on Langtang glacier. Within 533 days, cliffs can change significantly in size and shape. This reduced the efficiency of the calculation, since less cliff area could be used to measure the backwasting distance from the t_1 to t_2 cliff surface. This reduction in suitable cliff area hampers the validation of distributed models or comparison with Brun et al. (2016) using absolute backwasting distances or volumes, since these studies used the whole cliff area. The difference in area used in this research and the other studies will become smaller if the cliffs maintain a very similar geometry (as cliff 2 on Lirung) or are monitored more frequent. However, absolute backwasting/volume loss estimates from modelling studies can still be compared to results of this study if they validate using the same area as used here.

Brun et al. (2016) distinguished between melt in different melt seasons, which is not possible in this research where the time step covers two ablation seasons and one winter season. This unevenly distribution of seasons moreover causes an overestimation in the annual melt rate values, since melt is relatively higher in the ablation season than in the winter season.

Some additional uncertainties must be addressed for cliff-pond system 15. The cliff evolution patterns obtained from this system are more uncertain than cliff backwasting patterns for cliff 7 and 13. The cliffs of cliff-pond system 15 developed largely from debris-covered areas, while the cliff backwasting patterns at cliff 7 and 13 were measured from cliff to cliff. Therefore, the debris layer causes an additional error in the cliff evolution patterns that would be approximately equal or smaller than the average debris thickness of 1 m. Additionally, since the 2014 surface of cliff-pond system 15 exhibited a (partly debris-covered) irregular surface rather than only ice cliffs, the backwasting distances had to be calculated using normals from the 2015 cliff surface. As the cliffs in the expert judgement were assumed to melt perpendicular from the 2014 rather than the 2015 surface (within the horizontal plane), this causes an additional error. This error is higher for cliff system 15A that became more curved towards 2015 and causes the M3C2 distances to be a little bit more unstable in the lower section of cliff 15A and 15B.

The calculated slope and aspects of the cliff systems were important for the interpretation of cliff development, but must be used with caution. Steep cliff parts were represented by fewer pixels than flatter parts of equal area, which will make the average slope and aspect values more controversial.

6. Conclusions and recommendations

The ice cliffs studied on the Langtang glacier showed average backwasting of 15.4 m over the survey period of 533 days, containing two ablation seasons and one winter season. This corresponds to 10.5 m a^{-1} and is 13 times higher than the average melt on relatively flat debris-covered areas. Ice cliffs thus enhance glacier ablation considerably and this could be an explanation for the debris-cover anomaly as was found by recent studies.

This study used the M3C2 algorithm with a normal scale of 20 m and a horizontal lock for the normals along the average cliff backwasting direction to generate spatial backwasting patterns. The technique allowed for rapid generation of these patterns from UAV data, which could up to the present time only be generated by computationally intensive cliff backwasting models. The RMSE between the expert judgement and M3C2 distances was only 0.4 m, indicating that this methodology is not only fast but also accurate. Unconstrained normals perpendicular to the cliff surface caused totally misdirected measurements and additionally showed a large RMSE of 2.2 m. This study therefore found that ice cliffs do not melt perpendicular to both small and large-scale cliff surfaces using yearly time steps.

Ice cliff backwasting was very heterogeneous on the cliff surface, as well as between different cliffs. These variations could largely be explained by the role of supraglacial ponds and aspect, indicating that these are very important in ice cliff evolution and ablation. Supraglacial ponds strongly influenced backwasting patterns by thermal erosion, which caused high subaqueous melt and potentially calving. This process caused a negative melt gradient from cliff base to top observed at cliffs adjacent to a pond. The role of ponds must therefore be fully included in distributed modelling studies. However, a supraglacial pond is no guaranty for high ablation rates, as a cliff with a northern aspect adjacent to a pond revealed the lowest backwasting rate. Aspect was also a very important factor in controlling cliff ablation, as a trend of increased melt was found for cliffs deviating from the north(east). Aspect moreover controlled cliff persistence over the survey period, as north-facing cliff sections showed higher persistence than cliff sections facing west.

Average backwasting rates found on a cliff at Lirung glacier are similar to backwasting rates found by previous studies on the cliff. The M3C2 spatial backwasting patterns furthermore revealed to be useful for validating the patterns found by distributed modelling studies.

This study showed that the methodology developed here can be applied even on a large time step of 533 days. As the M3C2 distances are measured from cliff to cliff, the efficiency of the method strongly decreases when the cliff geometry changes considerable over a large time step. A small time step is therefore recommended for future work, emphasizing the need for more frequent UAV surveys. A higher temporal resolution of the UAV surveys could also reveal ablation processes that cannot be observed using larger time steps.

The methodology has much potential for spatial and temporal upscaling, since the M3C2 calculation can be executed in around 60 seconds on an average computer. Cliff alignment, delineation and rotation are most time consuming steps, but could theoretically all be automated. Alignment is in this research conducted manually per cliff system, but it could be automated using the frequency cross-correlation technique as implemented in the software COSI-corr (Leprince, Ayoub, Klinger, & Avouac, 2007). Cliff delineation and identification could be semi-automated by using the Object Based Image Analysis (OBIA) technique as in Kraaijenbrink et al. (2016). Once an automatization technique is developed for defining the best measurement direction, the generation of spatial backwasting patterns could be automatized. Backwasting patterns could then be generated rapidly for all cliffs on the UAV-monitored area of the Langtang and Lirung glacier. This upscaling could reveal important relationships between different cliff properties and observed backwasting and allows for an accurate estimation of the contribution of cliff melt to total glacier ablation, which could serve as an input for catchment scale hydrological models.

References

Agisoft LLC. (2014). Agisoft PhotoScan User Manual Professional Edition, Version 1.1. Retrieved 9 September 2016, from http://www.agisoft.com/pdf/photoscan-pro_1_1_en.pdf

Agrawala, S., Raksakulthai, V., Larsen, P., Smith, J., & Reynolds, J. (2003). Development and climate change in nepal: focus on water resources and hydropower. *Oecd*, 1–64. http://doi.org/10.1111/j.1475-4762.2009.00911.x

Barsch, D. (1992). Permafrost creep and rock glaciers. *Permafrost and Periglacial Processes*, *3*, 175–188.

Benn, D. I., Bolch, T., Hands, K., Gulley, J., Luckman, A., Nicholson, L. I., … Wiseman, S. (2012). Response of debris-covered glaciers in the Mount Everest region to recent warming, and implications for outburst flood hazards. *Earth-Science Reviews*, *114*(1–2), 156–174. http://doi.org/10.1016/j.earscirev.2012.03.008

Benn, D. I., Wiseman, S., & Hands, K. A. (2001). Growth and drainage of supraglacial lakes on debrismantled Ngozumpa Glacier, Khumbu Himal, Nepal. *Journal of Glaciology*.

Berthier, E., Schiefer, E., Clarke, G. K. C., Menounos, B., & Rémy, F. (2010). Contribution of Alaskan glaciers to sea-level rise derived from satellite imagery. *Nature Geoscience*, *3*(2), 92–95. http://doi.org/10.1038/ngeo737

Bolch, T. (2011). Debris. *Encyclopedia of Snow, Ice and Glaciers*.

Bolch, T., Buchroithner, M., & Pieczonka, T. (2008). Planimetric and volumetric glacier changes in the Khumbu Himal, Nepal, since 1962 using Corona, Landsat TM and ASTER data. *Journal of Glaciology*, *54*(187), 592–600.

Bolch, T., Kulkarni, A., Kaab, A., Huggel, C., Paul, F., Cogley, J. G., … Stoffel, M. (2012). The State and Fate of Himalayan Glaciers. *Science*, *336*(6079), 310–314. http://doi.org/10.1126/science.1215828

Bolch, T., Pieczonka, T., & Benn, D. I. (2011). Multi-decadal mass loss of glaciers in the Everest area (Nepal Himalaya) derived from stereo imagery. *Cryosphere*, *5*(2), 349–358. http://doi.org/10.5194/tc-5-349-2011

Brodu, N., & Lague, D. (2012). 3D point cloud classification of complex natural scenes using a multi-scale dimensionality criterion: applications in geomorphology. In *EGU General Assembly Conference Abstracts* (Vol. 14, p. 4368).

Brun, F., Buri, P., Miles, E. S., Wagnon, P., Steiner, J., Berthier, E., … Pellicciotti, F. (2016). Quantifying volume loss from ice cliffs on debris-covered glaciers using high-resolution terrestrial and aerial photogrammetry. *Journal of Glaciology*, *62*(234), 684–695. http://doi.org/10.1017/jog.2016.54

Buri, P., Miles, E. S., & Steiner, J. F. (2016b). A physically-based 3D-model of ice cliff evolution over debris-covered glaciers. *Journal of Geophysical Research: Earth Surface*. http://doi.org/10.1002/2016JF004039

Buri, P., Pellicciotti, F., Steiner, J. F., Miles, E. S., & Immerzeel, W. W. (2016a). A grid-based model of backwasting of supraglacial ice cliffs on debris-covered glaciers. *Annals of Glaciology*, *57*(71), 199–

211. http://doi.org/10.3189/2016AoG71A059

Cignoni, P., Rocchini, C., & Scopigno, R. (1998). Metro: Measuring Error on Simplfied Surfaces. *Compututer Graphics Forum, 17*(2), 167–174. http://doi.org/10.1111/1467-8659.00236

Eijpen, K., Warren, C., & Benn, D. (2003). Subaqueous melt rates at calving termini: a laboratory approach. *Annals of Glaciology.*

Gardelle, J., Berthier, E., & Arnaud, Y. (2012). Slight mass gain of Karakoram glaciers in the early twenty-first century. *Nature Geoscience, 5*(5), 322–325. http://doi.org/10.1038/ngeo1450

Gardelle, J., Berthier, E., Arnaud, Y., & Kääb, A. (2013). Region-wide glacier mass balances over the Pamir-Karakoram-Himalaya during 1999–2011. *The Cryosphere, 7*(4), 1263–1286. http://doi.org/10.5194/tc-7-1263-2013

Girardeau-Montaut, D. (2015). Cloud Compare version 2.6. 1-user manual. Retrieved 17 August 2016, from http://www.cloudcompare.org/doc/qCC/CloudCompare v2.6.1 - User manual.pdf

Hambrey, M. J., Quincey, D. J., Glasser, N. F., Reynolds, J. M., Richardson, S. J., & Clemmens, S. (2009). Sedimentological, geomorphological and dynamic context of debris-mantled glaciers, Mount Everest (Sagarmatha) region, Nepal. *Quaternary Science Reviews, 28*(11), 1084. http://doi.org/10.1016/j.quascirev.2009.04.009

Han, H., Wang, J., Wei, J., & Liu, S. (2010). Backwasting rate on debris-covered Koxkar glacier, Tuomuer mountain, China. *Journal of Glaciology, 56*(196), 287–296. http://doi.org/10.3189/002214310791968430

Immerzeel, W. . W., van Beek, L. P. H., Konz, M., Shrestha, A. B., & Bierkens, M. F. P. (2012). Hydrological response to climate change in a glacierized catchment in the Himalayas. *Climatic Change, 110*(3–4), 721–736. http://doi.org/10.1007/s10584-011-0143-4

Immerzeel, W. W., & Bierkens, M. F. P. (2012). Asia's water balance. *Nature Geoscience, 5*, 841–842. http://doi.org/10.1038/ngeo1643

Immerzeel, W. W., Kraaijenbrink, P. D. A., Shea, J. M., Shrestha, A. B., Pellicciotti, F., Bierkens, M. F. P., & Jong, S. M. De. (2014). High-resolution monitoring of Himalayan glacier dynamics using unmanned aerial vehicles. *Remote Sensing of Environment, 150*, 93–103. http://doi.org/10.1016/j.rse.2014.04.025

Immerzeel, W. W., Pellicciotti, F., & Bierkens, M. F. P. (2013). Rising river flows throughout the twenty-first century in two Himalayan glacierized watersheds. *Nature Geoscience, 6*(9), 742–745. http://doi.org/10.1038/ngeo1896

Immerzeel, W. W., van Beek, L. P. H., & Bierkens, M. F. P. (2010). Climate change will affect the Asian water towers. *Science (New York, N.Y.), 328*(5984), 1382–5. http://doi.org/10.1126/science.1183188

Jianchu, X., Shrestha, A., & Eriksson, M. (2009). Climate change and its impacts on glaciers and water resource management in the Himalayan Region. *Assessment of Snow, Glacier and Water Resources in Asia*, 43–54.

Jordan, R. E., & Stark, J. A. (2001). Capillary Tension in Rotting Ice Layers Cold Regions Research, (September).

Kääb, A., Berthier, E., Nuth, C., Gardelle, J., & Arnaud, Y. (2012). Contrasting patterns of early twenty-first-century glacier mass change in the Himalayas. *Nature, 488*(7412), 495–498. http://doi.org/10.1038/nature11324

Kääb, A., Treichler, D., Nuth, C., & Berthier, E. (2015). Brief Communication: Contending estimates of 2003-2008 glacier mass balance over the Pamir-Karakoram-Himalaya. *Cryosphere, 9*(2), 557–564. http://doi.org/10.5194/tc-9-557-2015

Kirkbride, M. (2011). Debris-covered glaciers. In *Encyclopedia of Snow, Ice and Glaciers* (pp. 190–192). http://doi.org/10.1007/978-90-481-2642-2

Kirkbride, M. P. (1993). The temporal significance of transitions from melting to calving termini at glaciers in the central Southern Alps of New Zealand. *The Holocene, 3*(3), 232–240. http://doi.org/10.1177/095968369300300305

Kraaijenbrink, P. D. A., Shea, J. M., Pellicciotti, F., de Jong, S. M., & Immerzeel, W. W. (2016). Object-based analysis of unmanned aerial vehicle imagery to map and characterise surface features on a debris-covered glacier. *Remote Sensing of Environment, 186*, 581–595.

Lague, D., Brodu, N., & Leroux, J. (2013). Accurate 3D comparison of complex topography with terrestrial laser scanner: Application to the Rangitikei canyon (N-Z). *ISPRS Journal of Photogrammetry and Remote Sensing.* http://doi.org/10.1016/j.isprsjprs.2013.04.009

Leprince, S., Ayoub, F., Klinger, Y., & Avouac, J.-P. (2007). Co-Registration of Optically Sensed Images and Correlation (COSI-Corr): an operational methodology for ground deformation measurements. In *2007 IEEE International Geoscience and Remote Sensing Symposium* (pp. 1943–1946). IEEE. http://doi.org/10.1109/IGARSS.2007.4423207

Lowe, D. G. (2004). Distinctive Image Features from Scale-Invariant Keypoints. *International Journal of Computer Vision, 60*(2), 91–110. http://doi.org/10.1023/B:VISI.0000029664.99615.94

Luckman, A., Quincey, D., & Bevan, S. (2007). The potential of satellite radar interferometry and feature tracking for monitoring flow rates of Himalayan glaciers. *Remote Sensing of Environment, 111*(2), 172–181. http://doi.org/10.1016/j.rse.2007.05.019

Lutz, A. F., Immerzeel, W. W., Shrestha, A. B., & Bierkens, M. F. P. (2014). Consistent increase in High Asia's runoff due to increasing glacier melt and precipitation. *Nature Climate Change, 4*(7), 587–592. http://doi.org/10.1038/nclimate2237

Miles, E. S., Pellicciotti, F., Willis, I. C., Steiner, J. F., Buri, P., & Arnold, N. S. (2016). Refined energy-balance modelling of a supraglacial pond, Langtang Khola, Nepal. *Annals of Glaciology, 57*(71), 29–40. http://doi.org/10.3189/2016AoG71A421

Nakawo, M. (2009). Shrinkage of summer-accumulation–glaciers in Asia under consideration of downstream population. In *Assessment of snow, glacier and water resources in Central Asia* (pp. 19–25).

Nakawo, M., & Young, G. J. (1981). Field experiments to determine the effect of a debris layer on ablation of glacier ice. *Annals of Glaciology, 2*(1), 85–91.

Nuimura, T., Fujita, K., Yamaguchi, S., & Sharma, R. R. (2012). Elevation changes of glaciers revealed by multitemporal digital elevation models calibrated by GPS survey in the Khumbu region, Nepal Himalaya, 1992-2008. *Journal of Glaciology, 58*(210), 648–656.
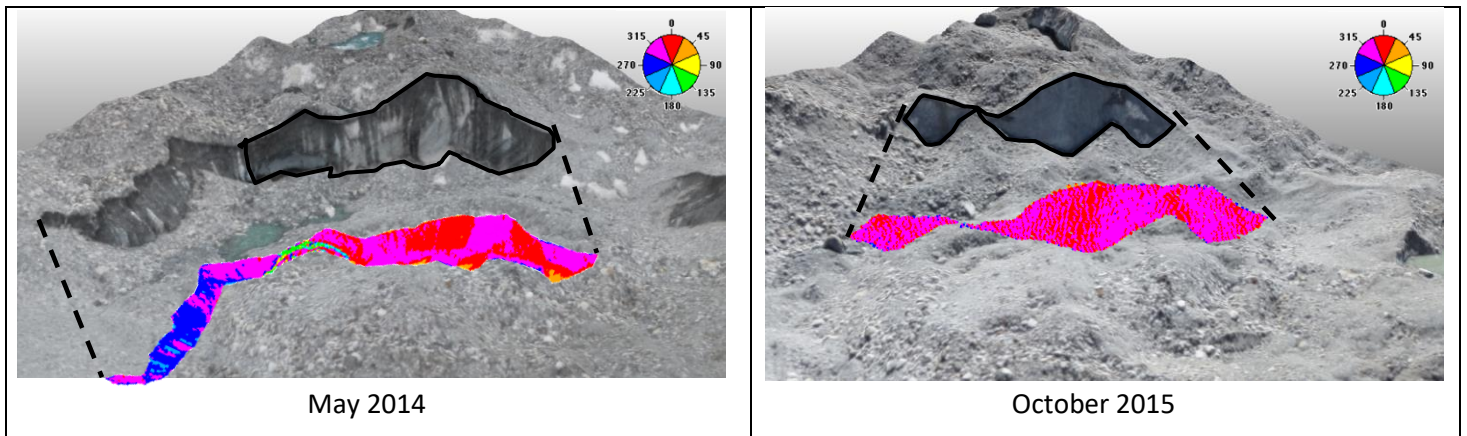
http://doi.org/10.3189/2012JoG11J061

Ogilvie, I. (1904). The effect of superglacial debris on the advance and retreat of some Canadian glaciers. *The Journal of Geology, 12*(8), 722–743.

Östrem, G. (1959). Ice Melting under a Thin Layer of Moraine, and the Existence of Ice Cores in Moraine Ridges. *Geografiska Annaler, 41*(4), 228–230. http://doi.org/10.2307/4626805

Pellicciotti, F., Stephan, C., Miles, E., Herreid, S., Immerzeel, W. W., & Bolch, T. (2015). Mass-balance changes of the debris-covered glaciers in the Langtang Himal, Nepal, from 1974 to 1999. *Journal of Glaciology, 61*(226), 373–386. http://doi.org/10.3189/2015JoG13J237

Quincey, D. J., Luckman, A., & Benn, D. (2009). Quantification of Everest region glacier velocities between 1992 and 2002, using satellite radar interferometry and feature tracking. *Journal of Glaciology, 55*(192), 596–606. http://doi.org/10.3189/002214309789470987

Ragettli, S., Bolch, T., & Pellicciotti, F. (2016). Heterogeneous glacier thinning patterns over the last 40 years in Langtang Himalaya. *The Cryosphere Discussion,* (February), 1–53. http://doi.org/10.5194/tc-2016-25

Rana, B., Masayoshi, N., Yutaka, A., Kubota, J., & Kojima, A. (1998). Glacier Ablation Under Debris Cover: Field Observations on Lirung Glacier, Nepal Himalayas. In *Proceedings of the International Conference on Ecohydrology of High Mountain Areas* (pp. 393–403).

Reid, T. D., & Brock, B. W. (2014). Assessing ice-cliff backwasting and its contribution to total ablation of debris-covered Miage glacier, Mont Blanc massif, Italy. *Journal of Glaciology, 60*(219), 3–13. http://doi.org/10.3189/2014JoG13J045

Rosser, N. J., Petley, D. N., Lim, M., Dunning, S. A., & Allison, R. J. (2005). Terrestrial laser scanning for monitoring the process of hard rock coastal cliff erosion. *Quarterly Journal of Engineering Geology and Hydrogeology, 38*(4), 363. http://doi.org/10.1144/1470-9236/05-008

Sakai, A., Nakawo, M., & Fujita, K. (1998). Melt rate of ice cliffs on the Lirung Glacier, Nepal Himalayas, 1996. *Bulletin of Glacier Research, 16*(October), 57–66.

Sakai, A., Nakawo, M., & Fujita, K. (2002). Distribution Characteristics and Energy Balance of Ice Cliffs on Debris-Covered Glaciers, Nepal Himalaya. *Arctic, Antarctic, and Alpine Research, 34*(1), 12. http://doi.org/10.2307/1552503

Sakai, A., Nishimura, K., Kadota, T., & Takeuchi, N. (2009). Onset of calving at supraglacial lakes on debris-covered glaciers of the Nepal Himalaya. *Journal of Glaciology, 55*(193), 909–917. http://doi.org/10.3189/002214309790152555

Sakai, A., Takeuchi, N., Fujita, K., & Nakawo, M. (2000). Role of supraglacial ponds in the ablation process of a debris-covered glacier in the Nepal Himalayas. *Debris-Covered Glaciers,* (264), 119–130.

Schaner, N., Voisin, N., Nijssen, B., & Lettenmaier, D. P. (2012). The contribution of glacier melt to streamflow. *Environmental Research Letters, 7*(3), 34029. http://doi.org/10.1088/1748-9326/7/3/034029

Scherler, D., Bookhagen, B., & Strecker, M. R. (2011). Spatially variable response of Himalayan glaciers to climate change affected by debris cover. *Nature Geoscience, 4*(3), 156–159.
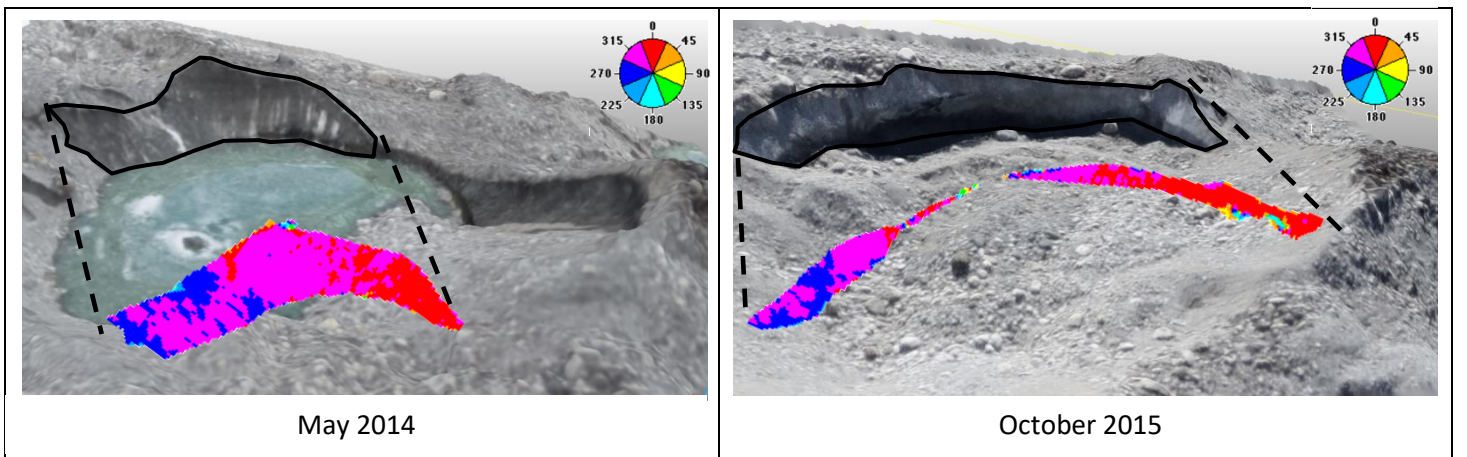
http://doi.org/10.1038/ngeo1068

Scott Watson, C., Quincey, D. J., Carrivick, J. L., & Smith, M. W. (2017). Ice cliff dynamics in the Everest region of the Central Himalaya. *Geomorphology*, *278*, 238–251. http://doi.org/10.1016/j.geomorph.2016.11.017

Seko, K., Yabuki, H., Nakawo, M., Sakai, A., Kadota, T., & Yamada, Y. (1998). Changing surface features of Khumbu Glacier, Nepal Himalaya revealed by SPOT images. *Bulletin of Glacier Research*, *16*, 33–41.

Sensefly. (2017). Ebee. The professional mapping drone. Retrieved from https://www.sensefly.com/drones/ebee.html

Sharma, K. P., Moore, B., & Vorosmarty, C. J. (2000). Anthropogenic, Climatic, and Hydrologic Trends in the Kosi Basin, Himalaya. *Climatic Change*, *47*(1/2), 141–165. http://doi.org/10.1023/A:1005696808953

Snavely, N. (2011). Scene Reconstruction and Visualization from Internet Photo Collections: A Survey. *IPSJ Transactions on Computer Vision and Applications*, *3*, 44–66. http://doi.org/10.2197/ipsjtcva.3.44

Steiner, J. F., Pellicciotti, F., Buri, P., Miles, E. S., Immerzeel, W. W., & Reid, T. D. (2015). Modelling ice-cliff backwasting on a debris-covered glacier in the Nepalese Himalaya. *Journal of Glaciology*, *61*(229), 889–907. http://doi.org/10.3189/2015JoG14J194

Suzuki, R. (2011). Debris Thermal Properties and Impact on Ice Ablation. *Encyclopedia of Snow, Ice and Glaciers*, 178–180.

Tangborn, W., & Rana, B. (2000). Mass Balance and runoff of the partially debris-covered Langtang Glacier, Nepal. *IAHS PUBLCATION*, (September), 99–108.

Wagnon, P., Vincent, C., Arnaud, Y., Berthier, E., Vuillermoz, E., Gruber, S., … Pokhrel, B. K. (2013). Seasonal and annual mass balances of Mera and Pokalde glaciers (Nepal Himalaya) since 2007. *Cryosphere*, *7*(6), 1769–1786. http://doi.org/10.5194/tc-7-1769-2013

Westoby, M. J., Brasington, J., Glasser, N. F., Hambrey, M. J., & Reynolds, J. M. (2012). 'Structure-from-Motion' photogrammetry: A low-cost, effective tool for geoscience applications. *Geomorphology*, *179*, 300–314. http://doi.org/10.1016/j.geomorph.2012.08.021

Appendix 1: 3D-overview of the selected cliff-pond systems

A: Cliff 7

May 2014

October 2015

B: Cliff 13

May 2014

October 2015

C: Cliff-pond system 15 (cliff 15A, 15B and 15C)

May 2014

October 2015
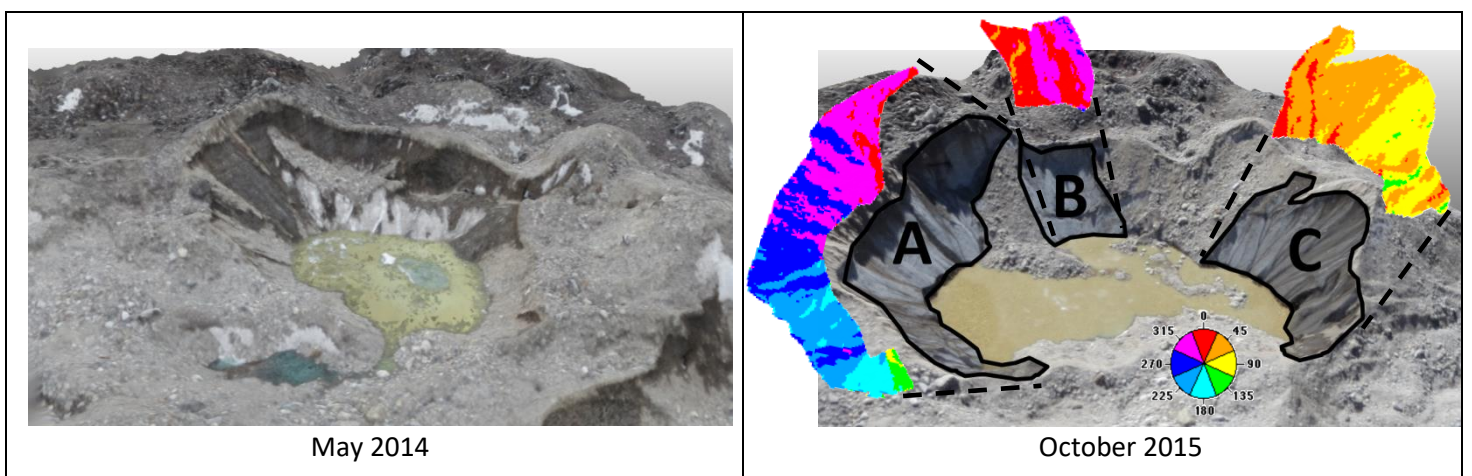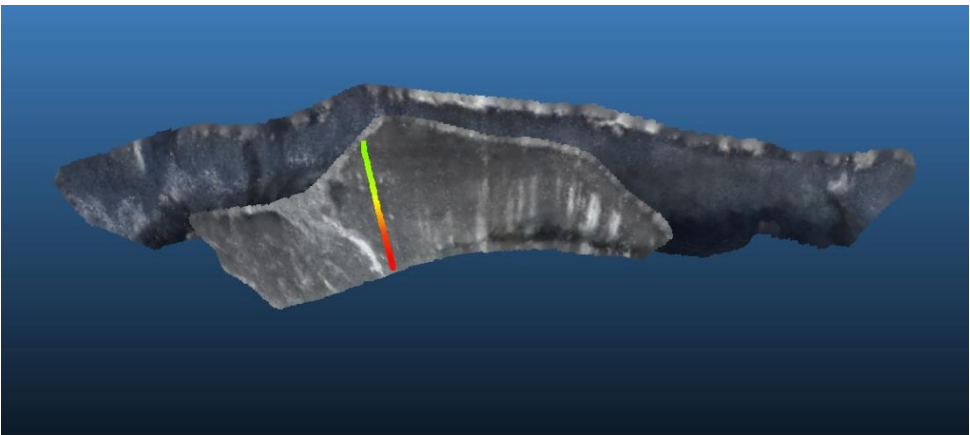
= Analysed cliff area

Appendix 2: 3D view of the delineated cliff areas and cross-sections used for the experiments

A: Cliff 7
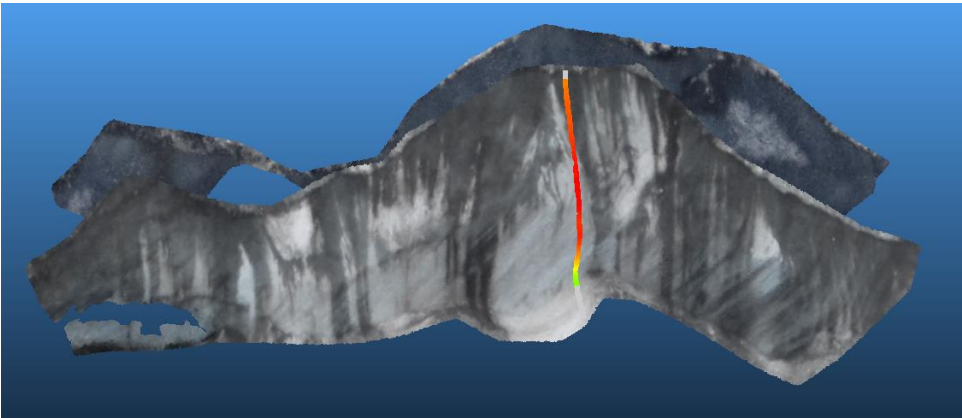
B: Cliff 13

C: Cliff 15A, B and C